Intrinsic origin of spin echoes in dipolar solids generated by strong π pulses

Dale Li, Yanqun Dong, R. G. Ramos, J. D. Murray, K. MacLean, A. E. Dementyev, and S. E. Barrett*
Department of Physics, Yale University, New Haven, Connecticut 06511, USA
(Received 26 April 2007; revised manuscript received 9 March 2008; published 24 June 2008)

In spectroscopy, it is conventional to treat pulses much stronger than the linewidth as delta functions. In NMR, this assumption leads to the prediction that π pulses do not refocus the dipolar coupling. However, NMR spin echo measurements in dipolar solids defy these conventional expectations when more than one π pulse is used. Observed effects include a long tail in the CPMG echo train for short delays between π pulses, an even-odd asymmetry in the echo amplitudes for long delays, an unusual fingerprint pattern for intermediate delays, and a strong sensitivity to π-pulse phase. Experiments that set limits on possible extrinsic causes for the phenomena are reported. We find that the action of the system's internal Hamiltonian during any real pulse is sufficient to cause the effects. Exact numerical calculations, combined with average Hamiltonian theory, identify terms that are sensitive to parameters such as pulse phase, dipolar coupling, and system size. Visualization of the entire density matrix shows a unique flow of quantum coherence from nonobservable to observable channels when applying repeated π pulses.

DOI: 10.1103/PhysRevB.77.214306 PACS number(s): 03.65.Yz, 03.67.Lx, 76.20.+q, 76.60.Lz

I. INTRODUCTION

Pulse action is crucial for many fields of study such as nuclear magnetic resonance (NMR), electron spin resonance, magnetic resonance imaging, and quantum information processing. In these fields, approximating a real pulse as a delta function with infinite amplitude and infinitesimal duration is a common practice when the pulses are much stronger than the spectral width of the system under study.[1–6] Delta-function π pulses, in particular, play a key role in bang-bang control,[7] which is an important technique designed to isolate qubits from their environments.[8–12]

In real experiments, all pulses are finite in amplitude and have nonzero duration. Nevertheless, for pulse sequences with a large number of $\pi/2$ pulses,[13,14] such as in NMR line-narrowing sequences,[3,5,15–19] using the delta-function pulse approximation yields qualitatively correct predictions. Furthermore, a more rigorous analysis that includes finite pulse effects only introduces relatively small quantitative corrections.[3] For this reason, reports[20–25] of finite pulse effects in dipolar solids including ^{29}Si in silicon, ^{13}C in C_{60}, ^{89}Y in Y_2O_3, and electrons in Si:P are surprising. In all of these studies, multiple high-powered π pulses much stronger than both the spread of Zeeman energies and the dipolar coupling were used; yet, the delta-function pulse approximation failed to predict the observed behavior.

By using exact numerical calculations and average Hamiltonian analysis, we show that the action of time-dependent terms during a nonzero duration π pulse is sufficient to cause many surprising effects, which is in qualitative agreement with experiments. Unfortunately, the complications and limitations of our theoretical approaches prevent us from providing a quantitative explanation of the experimental results, as we will explain below. We hope that an improved theory and new experiments will close the gap and enable a quantitative test of the model.

We initially set out to measure the transverse spin relaxation time T_2 for both ^{31}P and ^{29}Si in silicon[26–30] doped with phosphorus, which is motivated by proposals to use spins in semiconductors for quantum computation.[31–36] In doing so, we discovered a startling discrepancy between two standard methods of measuring T_2 using the NMR spin echo.[1]

The first method is the Hahn echo (HE), where a single π pulse is used to partially refocus magnetization,[37]

$$\mathrm{HE}: 90_X - \tau - 180_Y - \tau - \mathrm{echo}.$$

The pulses are represented as their intended rotation angle with their phase as subscripts. For this sequence, each Hahn echo [Fig. 1(dots)] is generated with a different time delay τ.

The second method is the Carr–Purcell–Meiboom–Gill (CPMG) echo train,[38,39]

$$\mathrm{CPMG}: 90_X - \tau - \{180_Y - \tau - \mathrm{echo} - \tau\}^n,$$

where the block in brackets is repeated n times for the nth echo. Note that CPMG is identical to HE for $n=1$. In contrast to the series of Hahn echo experiments, the CPMG echo train [Fig. 1 (lines)] should give T_2 in a single experiment.

As Fig. 1 shows, the T_2 inferred from the echo decay is strikingly different depending on how it is measured. Admittedly, two different experiments that give two different results is not uncommon in NMR. In fact, in liquid state NMR, the CPMG echo train is expected to persist after the Hahn echoes have decayed to zero. In the liquid state, spins can diffuse to different locations in a static inhomogeneous magnetic field.[1,6,38] This diffusion leads to a time-dependent fluctuation in the local field for individual spins, which spoils the echo formation at long τ. By rapidly pulsing a liquid spin system, it is possible to render these diffusive dynamics quasistatic. In this case, the coherence from one echo to the next is maintained by resetting the start of the precession at each echo. As a consequence, the CPMG echo train can approach the natural diffusion-free T_2 limit. In contrast, the Hahn echo experiment with only one refocusing pulse can decay faster due to diffusion. However, in the solids studied here, the lack of diffusion makes the local field time independent so the Hahn echoes and CPMG echo train are expected to agree, at least for delta-function π pulses.

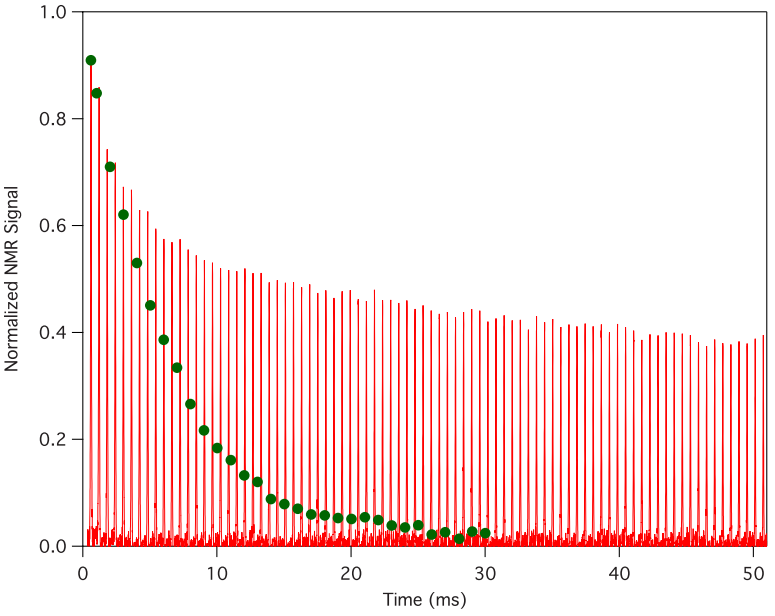

FIG. 1. (Color online) Two NMR experiments to measure T_2 of ^{29}Si in a crushed powder of Silicon doped with phosphorus (3.94×10^{19} P/cm^3). Hahn echo peaks (dots) are generated with a single π pulse. The CPMG echo train (lines) is generated with multiple π pulses spaced with delay $2\tau=592$ μs. Normalization is set by the initial magnetization after the 90_X pulse. Data taken at room temperature in a 12 T field.

The expected behavior of the CPMG sequence can be modeled by using the density matrix $\rho(t)$, which represents the full quantum state of the system.[1,4] The time evolution of the density matrix is expressed as

$$\rho(t) = \{\mathcal{V}\mathcal{P}\mathcal{V}\}^n \rho(0) \{\mathcal{V}^{-1}\mathcal{P}^{-1}\mathcal{V}^{-1}\}^n, \quad (1)$$

where n is the number of π pulses applied. The total evolution time $t=n(2\tau+t_p)$ depends on τ, the duration of the free-evolution period under $\mathcal{V}$, and t_p, the duration of the pulse period under $\mathcal{P}$. The form of the unitary operators $\mathcal{P}$ and $\mathcal{V}$ are not yet specified, so while Eq. (1) is complete, it is not yet very useful.

Section II outlines methods of calculating the evolution of $\rho(t)$ by using the delta-function pulse approximation for $\mathcal{P}$ and the Zeeman and dipolar Hamiltonians for $\mathcal{V}$. By using these approximations, the Hahn echoes and the CPMG echo train decay identically.

Section III summarizes experiments where multiple π pulse sequences grossly deviate from the expectations of Sec. II. In addition to the discrepancy shown in Fig. 1, observed effects include an even-odd asymmetry between the heights of even-numbered echoes and odd-numbered echoes when τ becomes large, a repeating fingerprint in subsets of the CPMG echo train for intermediate τ, and a sensitivity of the echo train to π pulse phase.

Section IV details many experiments that explore extrinsic effects in the pulse quality and the total system Hamiltonian. Specifically, we sought to understand our real pulse $\mathcal{P}$ as it differs from the idealized delta-function pulse. Studies include the analysis of the nutation experiment, tests of rf field inhomogeneity, measurement of pulse transients, dependence of effects on pulse strength, and improvements through composite pulses. Additionally, we looked for contributions to the free evolution $\mathcal{V}$ besides the dipolar coupling and Zeeman interaction by studying nonequilibrium effects, temperature effects, different systems of spin-1/2 nuclei, a single crystal, and magic angle spinning.

Section V presents a series of numerical simulations by using a simplified model based on the constraints imposed by the experiments of Sec. IV. These calculations qualitatively reproduce the long-lived coherence in CPMG and the sensitivity on π pulse phase. In order to get these results with $N=6$ spins, the simulations assumed both larger linewidths and shorter τ than in the experiments. A comparison of simulations with different N suggests that similar results could be obtained with smaller linewidths and longer τ provided that N is increased beyond the limits of our calculations. For insight into the physics of the exact calculations, the pulse sequences are analyzed by using average Hamiltonian theory. From this analysis, special terms are identified that contribute to the extension of measurable coherence in CPMG simulations with strong but finite pulses. Furthermore, the CPMG echo train tail height is sensitive to the total number of spins that are included in the calculation. This dependence on system size suggests that real pulses applied to a macroscopic number of spins may lead to the observed behaviors in Fig. 1 and Sec. III.

Section VI visualizes the entire density matrix to show the effects of the new terms identified in Sec. V. Regions of the density matrix that are normally inaccessible in the delta-function pulse approximation are connected to the measurable coherence by novel quantum coherence transfer pathways that play an important role in the CPMG long-lived tail, as simulated in Sec. V.

II. CALCULATED EXPECTATIONS FROM INSTANTANEOUS π PULSES AND DIPOLAR EVOLUTION

In this section, we calculate the expected behavior of N spin-1/2 particles under the action of pairwise dipolar coupling and instantaneous π pulses to compare with the experimental results of Fig. 1.

A. Internal spin hamiltonian

In order to calculate the expected behavior, we first write the relevant internal Hamiltonian for the system. The ideal

Hamiltonian for a solid containing N spin-1/2 nuclei in an external magnetic field contains two parts.[1–3] In the laboratory frame, the Zeeman Hamiltonian

$$\mathcal{H}_Z^{\text{lab}} = \sum_{j=1}^{N} -\gamma\hbar(B^{\text{ext}} + \Delta B_j^{\text{loc}})I_{z_j} \tag{2}$$

describes the interaction with the applied and local magnetic fields, while the dipolar Hamiltonian

$$\mathcal{H}_d^{\text{lab}} = \sum_{j=1}^{N}\sum_{k>j}^{N}\left[\frac{\vec{\mu}_j\cdot\vec{\mu}_k}{|\vec{r}_{jk}|^3} - \frac{3(\vec{\mu}_j\cdot\vec{r}_{jk})(\vec{\mu}_k\cdot\vec{r}_{jk})}{|\vec{r}_{jk}|^5}\right] \tag{3}$$

describes the interaction between two spins. In these Hamiltonians, γ is the gyromagnetic ratio and B^{ext} is an external magnetic field applied along $\hat{z}$. For spin j, ΔB_j^{loc} is the local magnetic field, $\vec{\mu}_j = \gamma\hbar\vec{I}_j$ is the magnetic moment, and $\vec{I}_j = (I_{x_j}, I_{y_j}, I_{z_j})$ is the spin angular momentum vector operator. The position vector between spins j and k is $\vec{r}_{jk}$.

We proceed to the rotating reference frame[1–3] defined by the Larmor precession frequency $\omega_0 = \gamma B^{\text{ext}}$. The Zeeman term largely vanishes leaving only a small Zeeman shift due to spatial magnetic inhomogeneities. The Zeeman shift for spin j is defined as $\Omega_{z_j} = -\hbar\gamma\Delta B_j^{\text{loc}}$. The scale of the spread of Zeeman shifts depends on the sample. For highly disordered samples or samples with magnetic impurities, Ω_{z_j} wildly varies between adjacent spins. The samples studied in this paper are much more spatially homogeneous, so Ω_{z_j} is essentially the same for a large number of neighboring spins. We therefore drop the index j giving the Zeeman Hamiltonian in the rotating frame,

$$\mathcal{H}_Z = \sum_{j=1}^{N}\Omega_z I_{z_j} = \Omega_z I_{z_T}, \tag{4}$$

where $I_{z_T} = \Sigma_{j=1}^{N} I_{z_j}$ is the total I_z spin operator. Strictly speaking, Eq. (4) can only describe a mesoscopic cluster of N spins (e.g., $N < 10$ are used in the numerical simulations), which share a single Ω_z value. We use an ensemble of N-spin clusters, varying Ω_z from one cluster to the next to simulate the macroscopic powders studied in this paper. The picture is that line broadening due to bulk diamagnetism will cause a spread in Ω_z values across a large sample (e.g., from one powder particle to the next) but that Ω_z will be nearly constant for most $N < 10$ spin clusters. Experiments that justify this assumption are presented in Sec. IV.

Even in the absence of the dipolar interaction, Zeeman shifts from different parts of the sample can cause signal decay, as shown in the Bloch sphere representation in Fig. 2. Each colored arrow represents a group of spins that experience a different ΔB^{loc} resulting in a slightly different precession frequency $\Omega_z/\hbar$ in the rotating frame. The initial magnetization at equilibrium starts aligned along the z axis [Fig. 2(a)]. After a 90_X pulse, the spins are tipped along the y axis [Fig. 2(b)]. Because of the spread of Zeeman shifts, spins in the rotating frame will begin to drift apart [Fig. 2(c)]. The resultant magnetization or vector sum will consequently decay [Fig. 2(d)]. This process is referred to as the free induction decay (FID) since it is detected in the NMR apparatus as

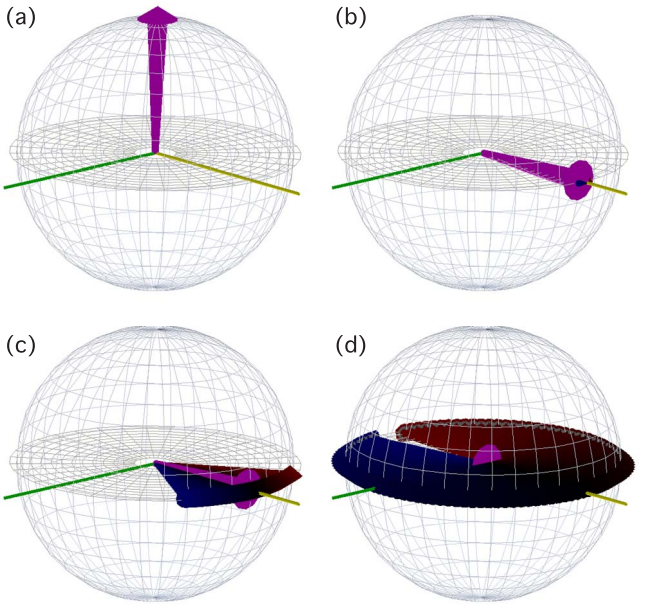

FIG. 2. (Color online) Bloch sphere depiction of signal decay due to a spread of Zeeman shifts. An external magnetic field is aligned along $\hat{z}$. (a) Spins in equilibrium with total magnetization represented by a large pink arrow. (b) After a 90_X pulse, the spins are aligned along $\hat{y}$ in the rotating frame. (c) Spins with different Zeeman shifts precess at different rates and fan apart. Red arrows represent spins with a positive Zeeman shift ($\Omega_z > 0$), blue arrows represent spins with a negative Zeeman shift ($\Omega_z < 0$), and black arrows represent spins on resonance ($\Omega_z = 0$). (d) After some time, the total magnetization decays to zero.

a decaying oscillatory voltage arising from magnetic induction in the detection coil.[1,40,41]

Even without a spread of Zeeman shifts across the sample, transverse magnetization will decay due to the dipolar coupling. It is appropriate to treat the dipolar Hamiltonian as a small perturbation[1] since the external magnetic field is typically 4 to 5 orders of magnitude larger than the field due to a nuclear moment. In this case, the secular dipolar Hamiltonian in the rotating frame is

$$\mathcal{H}_{zz} = \sum_{j=1}^{N}\sum_{k>j}^{N} B_{jk}(3I_{z_j}I_{z_k} - \vec{I}_j\cdot\vec{I}_k), \tag{5}$$

where the terms dropped from Eq. (3) are nonsecular in the rotating frame. We define the dipolar coupling constant as

$$B_{jk} \equiv \frac{1}{2}\frac{\gamma^2\hbar^2}{|\vec{r}_{jk}|^3}(1 - 3\cos^2\theta_{jk}), \tag{6}$$

where θ_{jk} is the angle between $\vec{r}_{jk}$ and $\vec{B}^{\text{ext}}$.

Thus, the relevant total internal spin Hamiltonian is

$$\mathcal{H}_{\text{int}} = \mathcal{H}_Z + \mathcal{H}_{zz}, \tag{7}$$

where we note that $\mathcal{H}_Z$ commutes with $\mathcal{H}_{zz}$. From this Hamiltonian, the free-evolution operator is defined as

$$\mathcal{U} \equiv e^{-(i/\hbar)\mathcal{H}_{\text{int}}\tau} = e^{-(i/\hbar)\mathcal{H}_Z\tau}e^{-(i/\hbar)\mathcal{H}_{zz}\tau} \equiv \mathcal{U}_Z\mathcal{U}_{zz}, \tag{8}$$

where $\mathcal{U}_Z$ and $\mathcal{U}_{zz}$ also commute.

B. Simplifying the external pulse

During the pulses, another time-evolution operator is needed. This pulse time-evolution operator is complicated since it contains all the terms in the free evolution plus an additional term associated with the rf pulse.

$$\mathcal{P}_\phi = \exp\left[-\frac{i}{\hbar}(\mathcal{H}_Z + \mathcal{H}_{zz} + \mathcal{H}_{P_\phi})t_p\right], \tag{9}$$

where

$$\mathcal{H}_{P_\phi} = -\hbar\omega_1 I_{\phi_T}, \tag{10}$$

for a radio frequency pulse with angular frequency ω_1 and transverse phase ϕ. In practice, the pulse strength and phase could vary from spin to spin. Studies of the effects of this type of rf inhomogeneity are reported in Sec. IV, but this approximate calculation considers the homogeneous case.

Note that $\mathcal{H}_{P_\phi}$, in general, does not commute with $\mathcal{H}_{\text{int}} = \mathcal{H}_Z + \mathcal{H}_{zz}$. Because of this inherent complication, it is advantageous to make ω_1 large so that $\mathcal{H}_{P_\phi}$ dominates $\mathcal{P}_\phi$. This strong-pulse regime is achieved when $\omega_1 \gg \Omega_z/\hbar$ and $\omega_1 \gg B_{jk}/\hbar$. This paper is primarily concerned with π pulses, which set the pulse duration t_p so that $\omega_1 t_p = \pi$. The delta-function pulse approximation[1–6] of a strong π pulse takes the limit $\omega_1 \to \infty$ and $t_p \to 0$ so that $\mathcal{P}_\phi$ simplifies to a pure left-handed π rotation

$$\mathcal{R}_\phi = \exp(i\pi I_{\phi_T}). \tag{11}$$

For these delta-function π pulses, the linear Zeeman Hamiltonian is perfectly inverted, while the bilinear dipolar Hamiltonian remains unchanged. The time-evolution operators thus transform as

$$\mathcal{R}_\phi \mathcal{U}_Z \mathcal{R}_\phi^{-1} = \mathcal{U}_Z^1, \tag{12}$$

$$\mathcal{R}_\phi \mathcal{U}_{zz} \mathcal{R}_\phi^{-1} = \mathcal{U}_{zz}. \tag{13}$$

In other words, after a π pulse, the Zeeman spread will refocus, while the dynamics due to dipolar coupling will continue to evolve as if the π pulse was never applied. Equation (13) is the basis for the statement: "π pulses do not refocus the dipolar coupling."

C. Analytic expression for the density matrix evolution in the instantaneous pulse limit

Using the free-evolution operator and the delta-function pulse, Eq. (1) for CPMG simplifies to

$$\begin{aligned}
\rho(t) &= \{\mathcal{U}R_y\mathcal{U}\}^n \rho(0) \{\mathcal{U}^{-1}\mathcal{R}_y^{-1}\mathcal{U}^{-1}\}^n \\
&= \{\mathcal{U}\mathcal{R}_y(\mathcal{R}_y^{-1}\mathcal{R}_y)\mathcal{U}(\mathcal{R}_y^{-1}\mathcal{R}_y)\}^n \rho(0) \{\text{inv}\}^n \\
&= \{\mathcal{U}_{zz}\mathcal{U}_Z\mathcal{U}_Z^1\mathcal{U}_{zz}\mathcal{R}_y\}^n \rho(0) \{\text{inv}\}^n \\
&= (\mathcal{U}_{zz})^{2n}(R_y)^n \rho(0)(R_y^{-1})^n (\mathcal{U}_{zz}^{-1})^{2n} \\
&= (\mathcal{U}_{zz})^{2n}\rho(0)(\mathcal{U}_{zz}^{-1})^{2n} = \mathcal{U}_{zz}(t)\rho(0)\mathcal{U}_{zz}^{-1}(t),
\end{aligned} \tag{14}$$

where {inv} is the inverse of the operators in brackets to the left of $\rho(0)$, the dipolar time-evolution operator for time t is $\mathcal{U}_{zz}(t) = \exp(-\frac{i}{\hbar}\mathcal{H}_{zz}t)$, and we assumed $(R_y)^n\rho(0)(R_y^{-1})^n = \rho(0) = I_{y_T}$. Invoking Eqs. (8), (12), and (13) has allowed the cancellation of $\mathcal{U}_Z$.

By assuming that the pulses are instantaneous, the density matrix at the time of an echo is independent of the Zeeman spread and the number of applied pulses. In other words, the peaks of the Hahn echoes and the CPMG echo train should follow the same decay envelope given by the dipolar-only ($\Omega_z = 0$) FID.

D. General method to calculate the observable NMR signal

The last step is to calculate the measured quantity that is relevant to our NMR experiments. The NMR signal is proportional to the transverse magnetization in the rotating reference frame.[1–6] Therefore, we wish to calculate

$$\langle I_{y_T}(t)\rangle = \sum_{j=1}^{N} \text{Tr}\{\rho(t) I_{y_j}\}. \tag{15}$$

The real experiment involves a macroscopic number of spins N but computer limitations force us to use only small clusters of coupled spins. Since the size of the density matrix grows as $2^N \times 2^N$, we are limited to $N < 10$.

To mimic a macroscopic system with only a small cluster of spins, we first built a lattice with the appropriate unit cell for the solid under study. Then, we randomly populated the lattice with spins according the natural abundance. For one spin at the origin, $N-1$ additional spins were chosen with the strongest coupling $|B_{1k}|$ to the central spin. Finally, we disorder averaged over many random lattice populations to sample different regions of a large crystal. For powder samples, we also disorder averaged over random orientations of the lattice with respect to $\vec{B}^{\text{ext}}$. This method is biased to make the central spin's local environment as realistic as possible since the dipole coupling falls off as $1/r^3$. We therefore chose to calculate $\langle I_{y_1}(t)\rangle$ for only the central spin in each disorder realization instead of $\langle I_{y_T}(t)\rangle$ for the entire cluster of spins.

By using these clusters, the time dependence of the density matrix is calculated by starting from its conventional Boltzmann equilibrium value

$$\rho_B = I_{z_T}, \tag{16}$$

assuming a strong B^{ext} and high temperature.[3] Treating a strong 90_X pulse as a perfect left-handed rotation about $\hat{x}$, ρ_B transforms as

$$\rho(0) = \mathcal{R}_{90_X}\rho_B\mathcal{R}_{90_X}^{-1} = I_{y_T}. \tag{17}$$

From this point, Eq. (14) gives the evolution for $\rho(t)$ in the limit of delta-function π pulses,

$$\rho(t) = \mathcal{U}_{zz}(t) I_{y_T} \mathcal{U}_{zz}^{-1}(t). \tag{18}$$

For each disorder realization (DR), the density matrix at time $t+dt$ is calculated by using the basis representation that diagonalizes the internal Hamiltonian. In this basis, the density matrix is given by the matrix formula

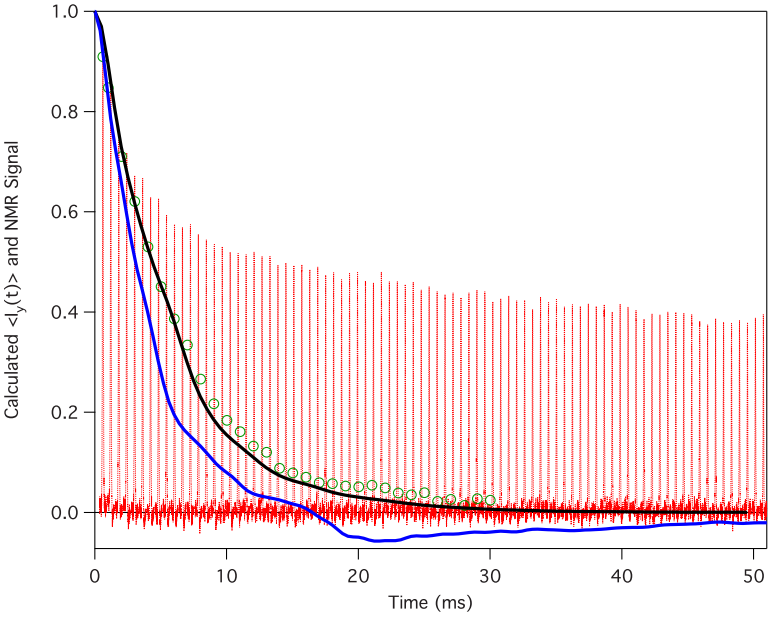

FIG. 3. (Color online) Expected decay curves for the delta-function pulse approximation using $\mathcal{H}_{zz}$ (blue curve) and $\mathcal{H}_{\mathrm{Ising}}$ (black curve). The blue curve uses clusters of $N=8$ spins and disorder averages over 1000 DRs. The black curve uses $N=80$ spins and averages over 20 000 DRs. Both calculations use the realistic silicon lattice (4.67% natural abundance of spin-1/2 ^{29}Si nuclei, diamond lattice constant 5.43 Å). Hahn echo data (green circles) and the CPMG echo train (dashed red lines) from Fig. 1 are plotted in the background for comparison.

$$\rho_{mn}(t+dt)=\rho_{mn}(t)e^{-(i/\hbar)(E_m-E_n)dt}, \tag{19}$$

where E_m is the mth eigenvalue of $\mathcal{H}_{zz}$ and ρ_{mn} is the element at the mth row and nth column of the $2^N\times 2^N$ density matrix.[1] By using the density matrix at each time t, the expectation value $\langle I_{y_1}(t)\rangle=\mathrm{Tr}\{\rho(t)I_{y_1}\}$ is calculated for each DR and then averaged over many DRs, yielding the expected decay for both CPMG and Hahn echoes [Fig. 3 (blue curve)].

Though $\mathcal{H}_{zz}$ is the appropriate Hamiltonian to consider, the small number of spins that we are able to treat can never describe the true dynamics of a macroscopic system even after substantial disorder averaging.

E. Ising model truncation

Let us consider another approach that truncates the secular dipolar Hamiltonian and yields an analytic expression for $\langle I_{y_1}(t)\rangle$ in the delta-function pulse limit. This truncation enables us to model the behavior of many more spins.

The secular dipolar Hamiltonian from Eq. (5) can be rewritten as

$$\mathcal{H}_{zz}=\sum_{j=1}^{N}\sum_{k>j}^{N}B_{jk}\left[2I_{z_j}I_{z_k}-\frac{1}{2}(I_j^+I_k^-+I_j^-I_k^+)\right] \tag{20}$$

by defining the raising and lowering operators

$$I^+=I_x+iI_y,$$

$$I^-=I_x-iI_y.$$

We call $I_j^+I_k^-$ and $I_j^-I_k^+$ the flip-flop terms. These terms flip one spin up and flop another spin down while conserving the total angular momentum.[1]

It is a very good approximation to drop the flip-flop terms whenever spins within a cluster have quite different Zeeman energies. In this case, the flip-flop would not conserve energy so this process is inhibited.[1] In this limit, $\mathcal{H}_{zz}$ is truncated to the Ising model Hamiltonian with long-range interactions,

$$\mathcal{H}_{\mathrm{Ising}}=\sum_{j=1}^{N}\sum_{k>j}^{N}2B_{jk}I_{z_j}I_{z_k}. \tag{21}$$

This approximation is usually made when considering the dipolar coupling between different spin species.[1] In the homonuclear systems that we consider, this approximation is not usually justified but we consider this limit here for comparison.

By using $\mathcal{H}_{\mathrm{Ising}}$, the product operator formalism[42] enables us to analytically evaluate $\langle I_{y_1}(t)\rangle$ for the central spin

$$\langle I_{y_1}(t)\rangle=I_{y_1}(0)\prod_{k>1}^{N}\cos(B_{1k}t/\hbar). \tag{22}$$

Since the expression in Eq. (22) is analytic,[40] the calculation of the resultant curve [Fig. 3 (black curve)] is not as computationally intensive as time evolving the entire density matrix. This calculation only requires the numerical value of the dipolar coupling B_{1k} between the central spin and a random population of $N-1$ spins on the lattice. In this way, many more spins can be treated. The final step is a disorder average over many random lattice occupancies and random lattice orientations.

Despite the differences in the two approaches, the simulated curves for the same lattice parameters are in reasonable agreement. The initial decay due to the secular dipolar Hamiltonian is two-thirds faster than the decay due to the Ising Hamiltonian in agreement with second-moment calculations.[1,40,43,44] The Hahn echo experiment in this sample follows the Ising model decay curve [Fig. 3 (green circles vs black curve)]. In other samples we have studied, the Hahn echo data lie between the calculated blue and black curves but always decay to zero. It is surprising then that the CPMG experiment has a measurable coherence well beyond the decay predicted by either approach [Fig. 3 (red lines)].

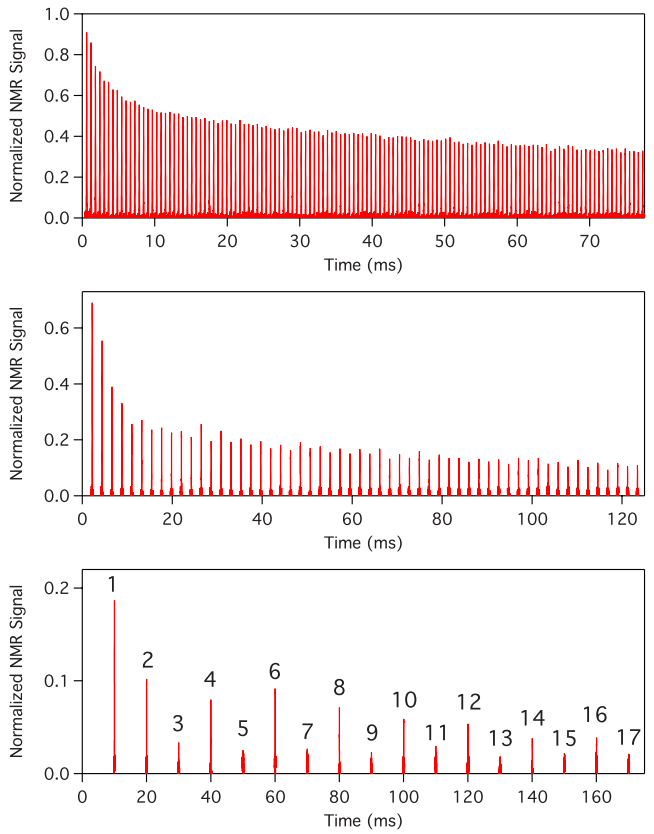

FIG. 4. (Color online) CPMG echo trains of ^{29}Si in Si:P (3.94×10^{19} P/cm^3) with three time delays between π pulses. (Top) $2\tau = 592$ μs. (Middle) $2\tau = 2.192$ ms. (Bottom) $2\tau = 9.92$ ms. For comparison, $T_2 = 5.6$ ms in silicon as measured by the Hahn echoes and as predicted by the delta-function pulse approximation. Data taken at room temperature in a 12 T field.

III. MORE EVIDENCE THAT CONTRADICTS THE DELTA-FUNCTION PULSE APPROXIMATION

We performed many NMR experiments on dipolar solids to try to illuminate different facets of the surprising results observed in Fig. 1. In this section, we summarize our most striking findings that are inconsistent with the expectations set by the delta-function pulse approximation.

Our first reaction to the long tail in the CPMG echo train was to assume that the π pulses were somehow locking the magnetization along our measurement axis.[13,45–50] Increasing the time delay τ between π pulses reduces the pulse duty cycle down to less than 0.04% but the NMR signal still did not exhibit the expected behavior. Figure 4 shows three CPMG echo trains with three different interpulse time delays. For short delays between π pulses, the CPMG echo train exhibits a long tail [Fig. 4 (top)]. For intermediate delays, some slight modulation develops in the echo envelope [Fig. 4 (middle)]. For much longer delays, we observe an even-odd effect where even-numbered echoes are much larger than odd-numbered echoes that occur earlier in time[20–22] [Fig. 4 (bottom)].

The slight modulation of the echo envelope for the middle graph of Fig. 4 is more visible when we perform the same CPMG experiment on a silicon sample with a lower doping. Figure 5 shows CPMG echo trains in Si:P (3×10^{13} P/cm^3) and Si:B (1.43×10^{16} B/cm^3). Here, the echo shape is much wider in time than for the higher doped Si:P (10^{19} P/cm^3) sample because the Zeeman spread is much smaller. The heights of the echoes in Fig. 5 modulate in a seemingly noisy way. However, when sampling short segments of echoes, an unusual fingerprint pattern repeatedly emerges throughout the echo train. Sections of the echo train are highlighted and overlapped to help guide the eyes. Figures 4 and 5 are evidence of complicated coherent effects.

From the analysis of Sec. II, the calculated envelope $|\langle I_{y_1}(t)\rangle|$ is expected to be insensitive to the π pulse phase. We define the following four pulse sequences:

$$\mathrm{CP}: 90_X - \tau - \{180_X - 2\tau - 180_X - 2\tau\}^n,$$

$$\mathrm{APCP}: 90_X - \tau - \{180_{\bar{X}} - 2\tau - 180_X - 2\tau\}^n,$$

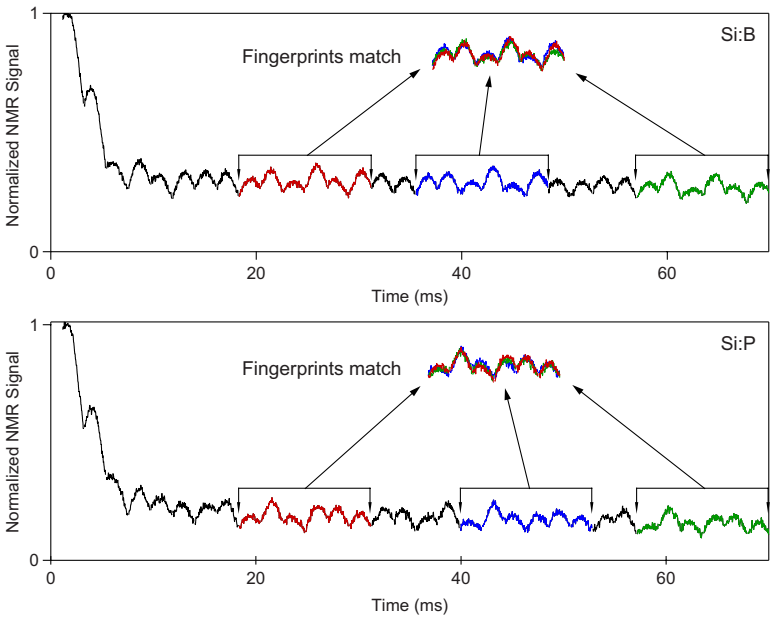

FIG. 5. (Color online) Repeated fingerprint patterns in the CPMG echo train with $2\tau = 2.192$ ms. Two different samples are shown: (top) Si:B (1.43×10^{16} B/cm^3), and (bottom) Si:P (3×10^{13} P/cm^3). Data taken at room temperature in a 7 T field.

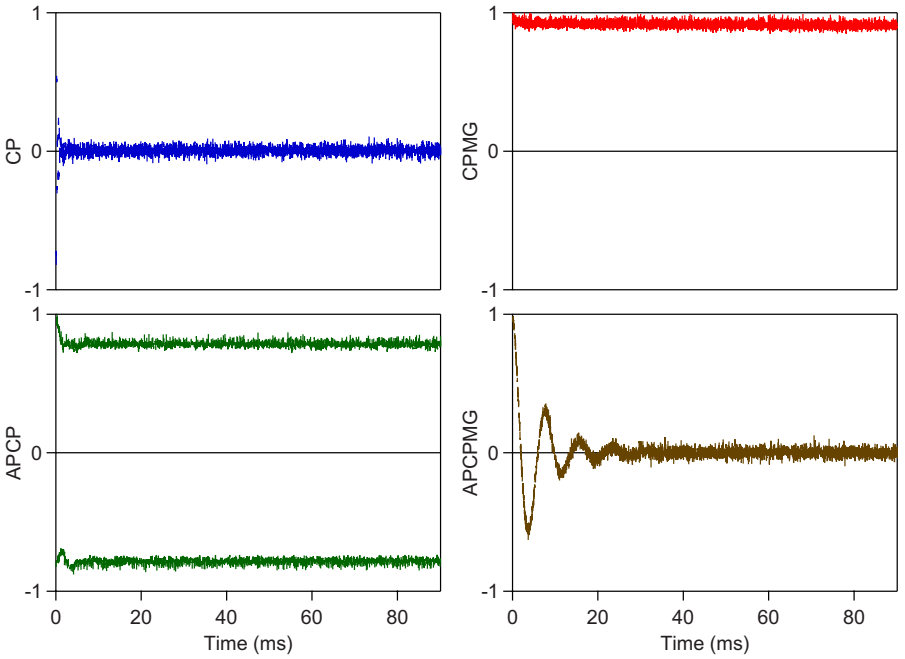

FIG. 6. (Color online) Four pulse sequences with π pulses of different phases applied to ^{29}Si in Si:Sb (2.75×10^{17} Sb/cm^3). (Top left) CP, (top right) CPMG, (bottom left) APCP, and (bottom right) APCPMG. All are expected to yield identical decay curves based on the delta-function pulse approximation. $2\tau=72$ μs, $T=300$ K, and $B^{\text{ext}}=11.74$ T.

$$\text{CPMG}: 90_X - \tau - \{180_Y - 2\tau - 180_Y - 2\tau\}^n,$$

$$\text{APCPMG}: 90_X - \tau - \{180_{\bar{Y}} - 2\tau - 180_Y - 2\tau\}^n,$$

where $\bar{X}$ indicates rotation about $-\hat{x}$ and $\bar{Y}$ indicates rotation about $-\hat{y}$. The Carr–Purcell (CP) sequence[38] features π pulses along $\hat{x}$, the CPMG sequence[39] features π pulses along $\hat{y}$, and the alternating phase (AP) versions flip the phase after each π pulse. The spin echoes form in the middle of each 2τ time period. For CP and APCP, the spin echoes alternatingly form along $\hat{y}$ and $-\hat{y}$, while in CPMG and APCPMG, they form only along $\hat{y}$. Though all of these sequences are expected to decay with the same envelope, they differ drastically in experiment (Fig. 6). The CP sequence decays extremely fast, while the APCP and CPMG sequences have extremely long-lived coherence. The pulse sequence sensitivity exhibited in Fig. 6 demonstrates that the π pulses play a key role in the system's response.

IV. EXPERIMENTAL TESTS TO UNDERSTAND THE PULSE QUALITY AND THE INTERNAL DYNAMICS OF THE SPIN SYSTEM

Because of the surprising results of the preceding section, we performed many experiments to test whether certain extrinsic factors were to blame for the discrepancies in Figs. 1 and 4–6. We report that even after greatly improving our experimental pulses, the tail of the CPMG echo train persists well beyond the decay of the Hahn echoes. We also report experiments with many different sample parameters that all yield the same qualitative result.

These experiments are quite different from the usual array of NMR experiments that primarily focus on optimizing the signal-to-noise ratio. In contrast, we have plenty of signal to observe in the CPMG echo train, but our aim was to find any sensitivity of the CPMG tail height on some extrinsic parameter. Although deliberately imposing a large pulse imperfection may lead to NMR data that look qualitatively similar to those outlined in the previous section, experimental improvements that greatly reduced these imperfections did not make the effects vanish.

A. Nutation calibration, rotary echoes, and pulse adjustments in Carr–Purcell–Meiboom–Gill

Without proper pulse calibration, it is difficult to predict the result of any NMR experiment. We calibrate the rotation angle of a real finite pulse through a series of measurements resulting in a nutation curve.[51] This experiment begins with the spins in the Boltzmann equilibrium $\rho_B=I_{z_T}$. During a square pulse of strength $H_1=\omega_1/2\pi$ and time duration t_{nut} applied along $\hat{x}$ in the rotating frame, the spins will nutate in the y-z plane. Shortly after t_{nut}, the projected magnetization along $\hat{y}$ is measured as the initial height of the FID.

Figure 7 shows a typical nutation curve in Si:Sb (2.75×10^{17} Sb/cm^3). The π pulse is determined by the timing of the first zero crossing of the nutation curve. This nutation calibration is typically repeated several times during a long experiment.

The nutation curve is also a measure of the quality of other aspects of the single-pulse experiment.[52] For example, the homogeneity of the applied rf field may be inferred from the decay of the nutation curve after several cycles. Figure 7 shows nutation data out to over eight cycles with very little decay. Extending the nutation experiment out to even longer pulse times (Fig. 8) enables the study of the decay of its amplitude.

For such long nutation times, the dipolar coupling between spins contributes to the decay.[53] This decay is calculated by using the density matrix evolved under the time-evolution operator for the full pulse [Eq. (9)] for time t_{nut}. The expected decay envelope [Fig. 8 (dashed curves)] is the

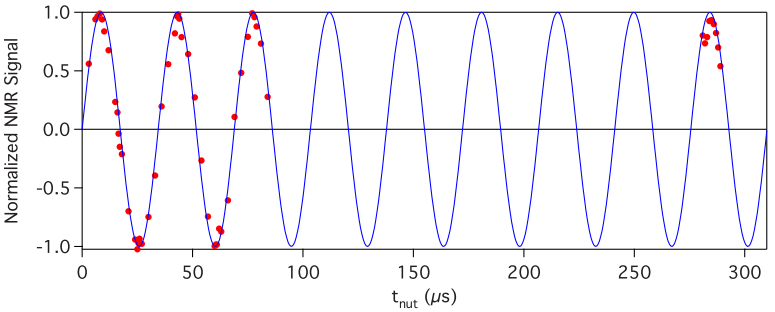

FIG. 7. (Color online) Nutation curve data (dots) of ^{29}Si in Si:Sb (2.75×10^{17} Sb/cm^3) agree with a nondecaying sine curve over 8.25 cycles. H_1=8.33 kHz, T=300 K, and B^{ext}=12 T.

disorder-averaged expectation value $\langle I_{y_1}(t)\rangle=\mathrm{Tr}\{\rho(t)I_{y_1}\}$ (see Sec. II).

Another significant contribution to the decay of the nutation curve is rf field inhomogeneity. For a given spread of rf fields, the decay of the NMR signal depends on the number of nutation cycles; therefore, a nutation with a weaker H_1 [Fig. 8 (top)] will decay slower than a nutation with a stronger H_1 [Fig. 8 (middle)]. The damped sine curves include the contribution from dipolar coupling and add the spatial rf field variations due to the calculated sample skin depth and the inherent inhomogeneities of our NMR coil.

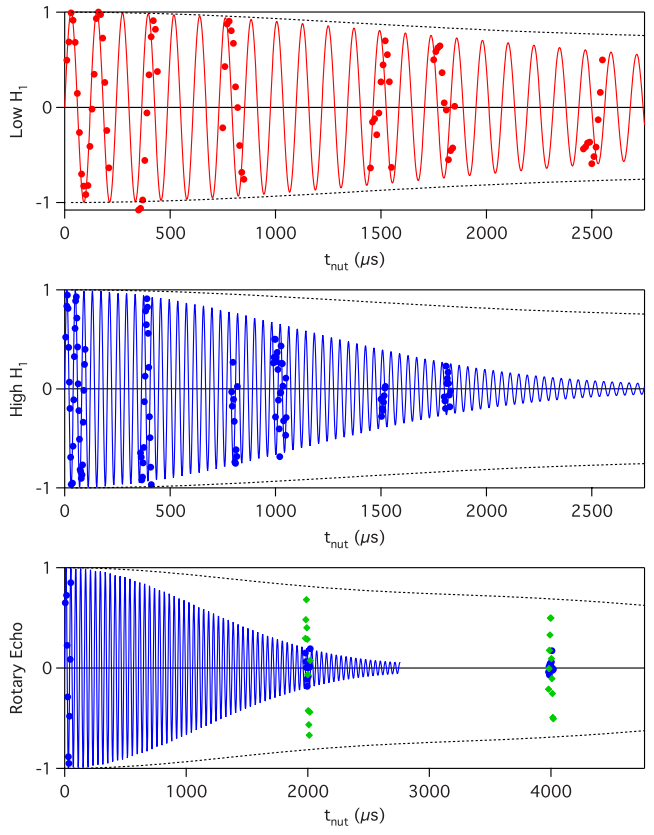

FIG. 8. (Color online) Extended nutation data of ^{29}Si in Si:Sb (2.75×10^{17} Sb/cm^3) taken at room temperature in a 12 T field. (Top) H_1=8.33 kHz. (Middle) H_1=25 kHz. (Bottom) Rotary echo data (green dots) and nutation data (blue dots) for H_1=25 kHz. Dashed lines in each graph show the expected decay envelope due to dipolar coupling during the nutation pulse. Solid traces are calculations that include the dipolar decay, rf field spread from our NMR coil, and skin depth of Si:Sb.

The rotary echo experiment[54] compensates for static spatial rf field inhomogeneities by reversing the phase of the nutation pulse at a time near $t_{\text{nut}}/2$. By using this technique, the rotary echo data [Fig. 8 (green dots)] approach the dipolar decay envelope even though the nutation data [Fig. 8 (blue dots)] decay much faster.

So far, the Hahn echoes, the nutation curve, and rotary experiment all agree with the model for calculating the NMR signal developed in Sec. II. One significant difference between these experiments and the CPMG sequence is that they consist of only one or two applied pulses while the CPMG sequence has many pulses. It is possible that the calibration for the CPMG sequence could be different than that set by the nutation curve. We explored this question of calibration by varying t_p of the π pulse to see if the expected decay would be recovered. Figure 9 (bottom) plots a series of echoes from the CPMG sequence versus the misadjusted π pulse duration. Spin echo 15 (SE15) and spin echo 16 (SE16) are representative of coherence that should decay to zero for delta-function π pulses. Despite the wide range of pulse durations attempted, the tail of the CPMG echo train never reached zero. Modifying CPMG with more complicated pulse phase patterns[55,56] changes the results, but echoes at long times are still observed.

B. Characterization of rf field homogeneity and improvements through sample modification

If the strength of the rf field during a pulse greatly varied from spin to spin, then the pulse calibration would not be consistent across the sample. To test whether this extrinsic effect could cause the results of Sec. III, we examined the rf field homogeneity in our NMR coil and made improvements by modifying the sample.

An ideal delta-function pulse affects all spins in the system with the same rf field strength. However, a real NMR coil is a short (approximately ten turn) solenoid with rf fields that vary in space.[57] Figure 10 shows a calculation of the rf field homogeneity in the quasistatic approximation by using the Biot–Savart law for our seven-turn NMR coil.[58,59] The grayscale plot indicates the spatial variation of rf fields where lighter colored regions are areas of higher rf field strength. The proximity effect would slightly smooth out these rf fields beyond what is shown.[57,60,61]

For a given coil, the rf field homogeneity can be improved by decreasing the sample volume. To this end, we performed experiments by using two different sample sizes to assess the influence of rf homogeneity on the long tail in the CPMG

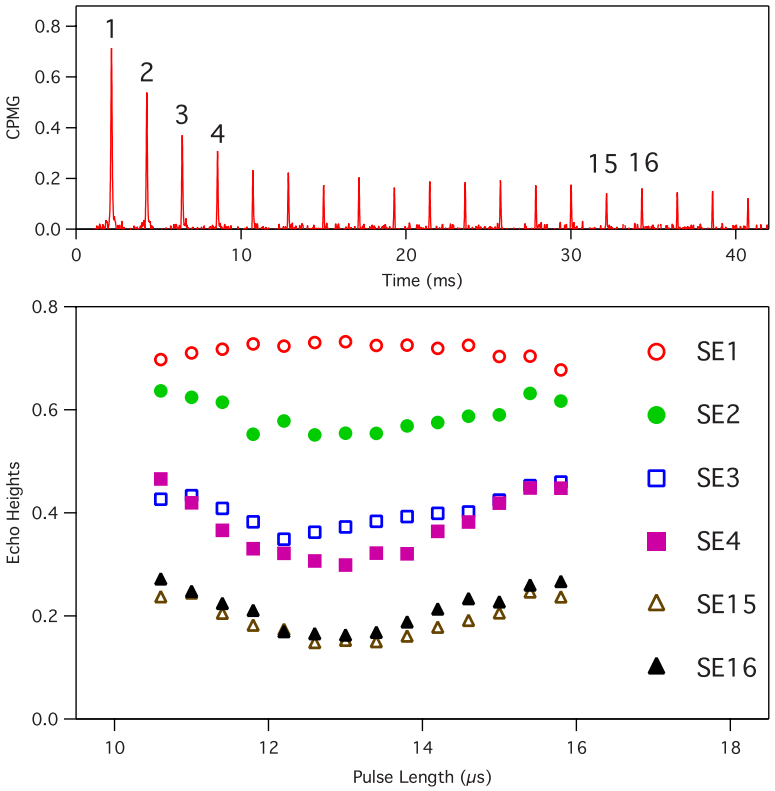

FIG. 9. (Color online) Finding the minimum tail height for CPMG. (Top) CPMG data of ^{29}Si in Si:P (3.94×10^{19} P/cm^3) with 2τ=2.192 ms. (Bottom) Numbered spin echoes (SEn) are plotted versus π pulse duration. SE15 and SE16 are expected to have zero amplitude. The nutation calibrated π pulse has duration 12.2 μs. Data taken at room temperature in a 12 T field.

echo train. Figure 10 shows histograms of the rf field distribution within the two sample sizes and the corresponding CPMG echo trains. No noticeable difference in the tail height was observed despite the marked improvement of rf homogeneity.

In addition to the coil dimensions, the sample itself may have properties that introduce an rf field inhomogeneity. For example, the skin depth in metallic samples attenuates the rf field inside the sample.[30,58,59] Two approaches were taken to reduce the contribution of skin depth effects to the rf field homogeneity. In the first approach, a sample of highly doped Si:P (10^{19} P/cm^3) was ground, passed through a 45 μm sieve, and diluted in paraffin wax. This high-doped silicon sample has a resistivity of 0.002 Ω cm. At a 12 T field, the rf frequency applied is 101.5 MHz. Thus, the skin depth at this frequency is 223.3 μm. Particle diameters on the order of 45 μm would only have a 10% reduction of the field at the center. Furthermore, dilution in wax helps to separate the particles. Despite this improvement, the effects summarized in Sec. III remained.

The second method to reduce the rf field attenuation caused by the skin depth is to use less metallic samples. Four different silicon samples were used that differ in dopant type (donors or acceptors) and dopant concentrations (up to a factor of a million less for Si:P with 10^{13} P/cm^3). For samples doped below the metal-insulator transition,[30] the calculated skin depth is very large and the rf field attenuation at the center of the particle is much smaller. For example, Si:Sb (2.75×10^{17} Sb/cm^3) has a skin depth of 1.05 mm, which reduces the H_1 field by 2% at the center of a 45 μm particle. Our lowest doped silicon powder sample, Si:P with 3×10^{13} P/cm^3 (resistivity of 0.97–2.90 Ω cm), has a skin depth range of 4.92–8.50 cm, which results in a less than 0.03% reduction in rf field at the particle center. Additionally, NMR measurements of ^{13}C in C_{60} and ^{89}Y in Y_2O_3, two which are insulating samples, show the same behavior as in silicon.[20–22]

Figure 11 shows the four pulse sequences in C_{60} for two sample sizes. Despite the improvement in rf field homogeneity, the long tail in the CPMG echo train and the pulse sequence sensitivity are largely unaffected.

C. Measuring the pulse transients

Pulse transients are another possible source of experimental error.[62–65] In principle, the perfect pulse is square and has a single rf frequency. In practice, however, the NMR tank circuit produces transients at the leading and trailing edges of the pulse. Because the pulse transients have both in-phase and out-of-phase components, they can cause spins to move out of the intended plane of rotation. These unintended transients can contribute to poor pulse calibration and possible accumulated imperfections. Therefore, it is important to quantify the pulse transients specific to our apparatus.

To measure the real pulse, we inserted a pickup loop near our NMR coil and applied our regular pulses.[62–64] Figure 12 shows the typical π pulse and $\pi/2$ pulse envelopes. The red traces show the in-phase components of the pulses, while the green traces show the out-of-phase components. Empirically, changing parameters such as the resonance and tuning of the NMR tank circuit changes the shape of the transients and even the sign of the out-of-phase components.

For short time pulses (e.g., a $\pi/2$ pulse), the transient constitutes a larger fraction of the entire pulse. Consequently, the dominant pulse transient in these short pulses could lead to larger extrinsic effects. Furthermore, since $H_1 t_p = 1/2$ is

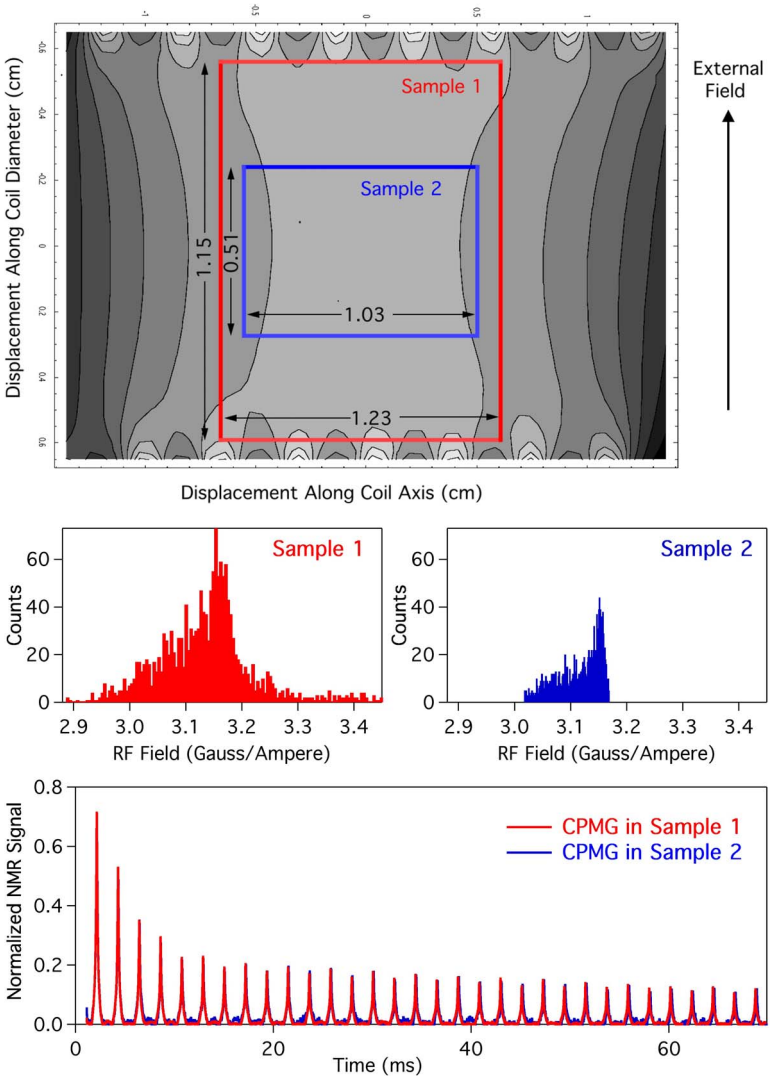

FIG. 10. (Color online) (Top) Sectional calculation of the rf field homogeneity in our NMR coil. Two cylindrical sample sizes are outlined. (Middle) Histograms of rf field strength distribution. (Bottom) CPMG data for the two sample sizes of ^{29}Si in Si:P (3.43×10^{19} P/cm^3) are nearly identical despite the noticeable change in rf field homogeneity. $2\tau=2.192$ ms, $T=300$ K, and $B^{\mathrm{ext}}=7$ T.

fixed for π pulses, one would expect that any extrinsic effects caused by pulse transients would also be larger for stronger (i.e., shorter in time) π pulses.

The influence of the pulse transients on the multiple-pulse sequences may be simulated[65] by approximating the real π pulse along $\hat{y}$ as a composite pulse of three pure rotations $180_Y\rightarrow4_{\bar{X}}180.1_Y3_X$. Including the pulse transients in simulation yielded only small changes in the expected decay envelope derived in Sec. II and could not reproduce the effects from Sec. III.

While the pulse transients are sensitive to many changes in our NMR apparatus, the observed effects from Sec. III are qualitatively insensitive. Therefore, we infer that the pulse transients are not the dominant cause of these effects.

D. Pulse strength dependence

How strong does a real pulse need to be in order to be considered a delta-function pulse? The limit described in Sec. II assumes pulses of infinite strength. This limit ensures that all the spins are identically rotated. On the other hand, weak pulses treat different spins differently. Thus, if the calibration, rf field homogeneity, or pulse strength was grossly misadjusted,[66] then the observed behavior could deviate from the calculation in Sec. II.

However, Fig. 13 shows CPMG experiments in Si:Sb (10^{17} Sb/cm^3) for a variety of pulse strengths. The tail height is extrapolated as a $t=0$ intercept from the CPMG pulse sequence [Fig. 13 (top)] and plotted versus the rf field strength $H_1=\omega_1/2\pi$ normalized by the full width at half maximum (FWHM) of the Si:Sb line shape. For each data point, a separate nutation curve was measured to calibrate the π pulse. The tail height of the CPMG echo train is largely insensitive to the pulse strength for H_1/FWHM from 4 to 450.

The expected CPMG decay may be simulated by using finite pulses[67] in an exact calculation for $N=5$ spins in silicon [Fig. 13 (bottom, open blue triangles)]. These calculations agree with the data when the pulses are extremely weak ($H_1/\mathrm{FWHM}<1$) but quickly fall to zero once the pulses are over ten times the linewidth. Thus, these calculations agree with the conventional assumption that the strong-pulse regime is achieved when $H_1/\mathrm{FWHM}\gg1$.

Because the experimental tail height in CPMG is so insensitive to large changes in pulse strength, we conclude that

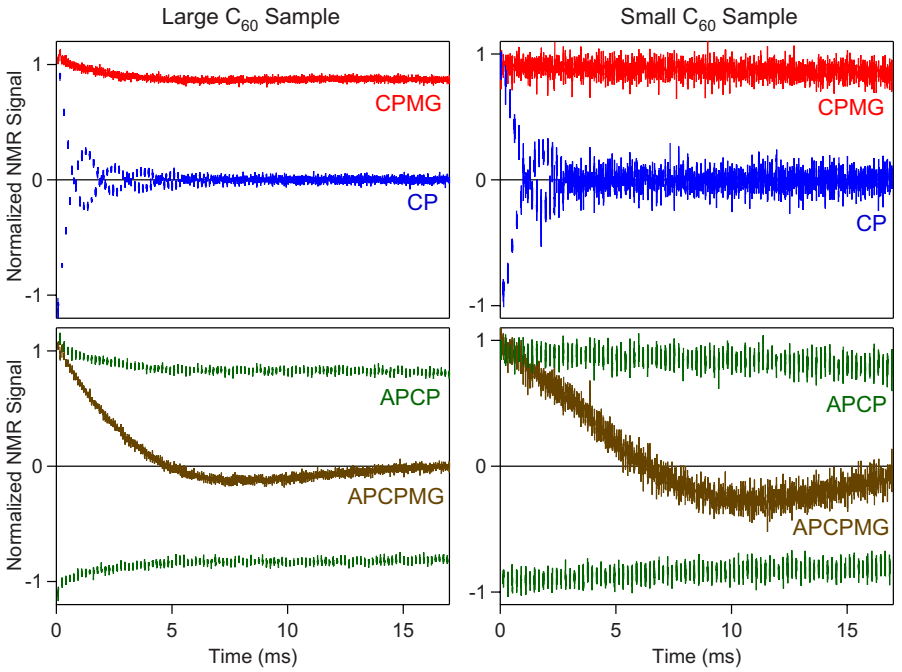

FIG. 11. (Color online) Pulse phase sensitivity and rf homogeneity tests in an insulating sample. CP, CPMG, APCP, and APCPMG data of ^{13}C in C_{60} for a large sample volume (left column) and a small sample volume (right column). All are expected to agree in the delta-function pulse limit. H_1 =45.5 kHz, ^{13}C NMR linewidth =290 Hz, 2τ=180 μs, T=300 K, and B^{ext}=12 T.

even very strong π pulses are still not the same as delta-function pulses.

E. Using composite π pulses to improve pulse quality

Another way to improve pulse quality is to use composite pulses[4,6,68] in place of single π pulses. Composite pulses were designed to correct poor pulse angle calibration, rf inhomogeneity, and the effects of weak pulses[69] by splitting a full rotation into separate rotations about different axes. These separate pieces counteract pulse imperfections when strung together.

Figure 14 shows a series of experiments where the single π pulses in CP, APCP, CPMG, and APCPMG are replaced by composite pulses. The Levitt composite pulse[68,70] replaces 180_Y with $90_X180_Y90_X$. The BB1 composite pulse[71,72] replaces 180_Y with $180_\alpha360_\beta180_\alpha180_Y$, where X=0°, Y=90°, α=194.5°, and β=43.4°. Even though these composite pulses should improve pulse quality,[71] the CPMG tail height and the sensitivity to π pulse phase are hardly affected.

F. Absence of nonequilibrium effects

This experiment tests the assumption made in Sec. II that the equilibrium density matrix is simply $\rho_B=I_{z_T}$. This ρ_B assumes that equilibrium is reached after waiting longer than the spin-lattice relaxation time T_1 before repeating a CPMG sequence.[1] If, however, an experiment is started out of equilibrium, then any unusual coherences[73,74] present in the initial density matrix might lead to a different NMR signal.

Figure 15 shows the CPMG echo train in two regimes. In red, the CPMG echo train is repeated after waiting only a fifth of the spin-lattice relaxation time T_1. In blue, the CPMG echo train is repeated after waiting $5\times T_1$. Inset (a) shows the saturation-recovery data that determines T_1. A single exponential is a good fit to the data supporting the assumption of a single mechanism for spin-lattice relaxation. Inset (b) shows a close-up of echoes for the two wait times. For shorter wait times, the echo shape is slightly distorted at the base of the echoes compared to the much longer wait times.

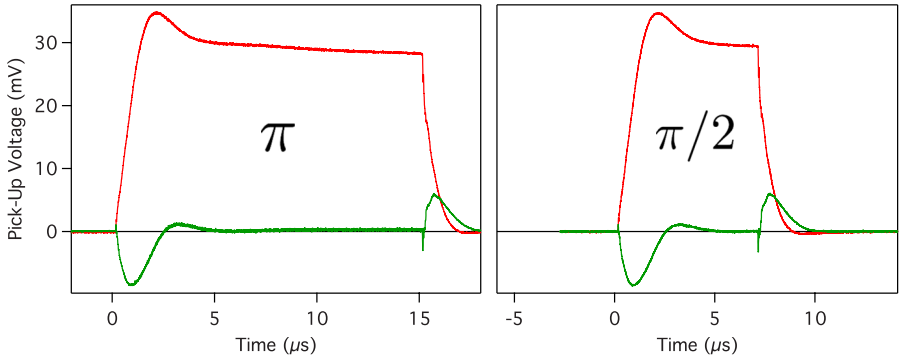

FIG. 12. (Color online) Measured pulse shapes in phase (red) and out of phase (green) for a typical π pulse (left) and $\pi/2$ pulse (right) at radio frequency 101.5 MHz with pulse strength H_1=33.3 kHz. Transients are a larger fraction of short duration pulses like $\pi/2$. Data taken at room temperature in a 12 T field. The real π pulse is approximated as three pure rotations $4_{\bar{X}}180.1_Y3_X$.

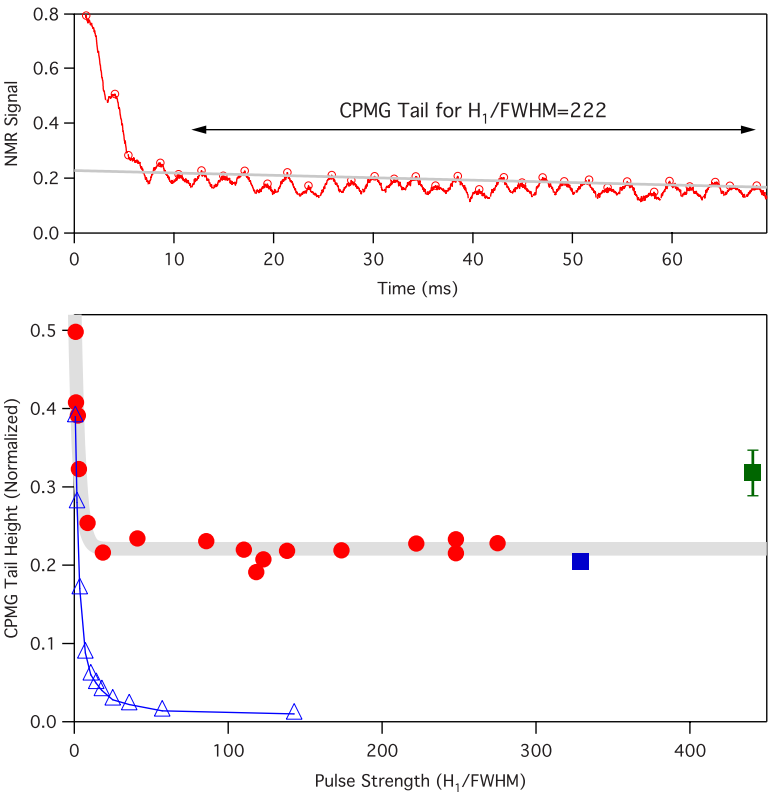

FIG. 13. (Color online) Dependence of CPMG tail height on pulse strength. (Top) Tail height is extrapolated as a $t=0$ intercept for CPMG of ^{29}Si in Si:Sb (2.75×10^{17} Sb/cm^3) with $2\tau=2.192$ ms. This example is for $H_1/\mathrm{FWHM}=222$. (Bottom) CPMG tail height versus pulse strength. Smaller samples and NMR coils were used to achieve the last two points. Exact calculations for $N=5$ spins in silicon (triangles) decay to zero for $H_1 \gg \mathrm{FWHM}$.

However, the CPMG echo peaks still exhibit a long tail and is insensitive to the wait time.

G. Absence of temperature dependence

The CPMG tail height could be sensitive to both temperature-dependent effects specific to each sample and temperature-independent effects found in all dipolar systems. To distinguish between the two sets of effects, we performed the CPMG pulse sequence in Si:P (3.94×10^{19} P/cm^3) at room temperature and at 4 K. Figure 16 shows that the CPMG tail height is insensitive to the large change in temperature.

These results update previously reported data in the same sample.[21] Lowering the temperature increases the spin-lattice relaxation time T_1 from 4.9 s at room temperature to over 6 h at 4 K. As a consequence, the increased T_1 at low temperatures required us to perform experiments at a much slower rate where our NMR tank circuit would be susceptible to temperature instabilities. These temperature instabilities caused poor pulse calibration from time to time. To rectify this problem, we repeated the CPMG pulse sequence many times at 4 K and measured the nutation curve after each repetition. If the calibration remained consistent between four applications of the CPMG pulse sequence, we averaged the four scans together to obtain the 4 K data in Fig. 16 (blue squares). None of these issues were present in the room temperature data.

In addition, the sample was carefully prepared by sieving the crushed powder to <45 μm and diluting it in paraffin wax to reduce the skin depth effect and to reduce clumping when cooling in a bath of liquid helium.

Absence of temperature dependence supports the assumption that the relevant internal Hamiltonian is $\mathcal{H}_{\mathrm{int}}=\mathcal{H}_Z+\mathcal{H}_{zz}$.

H. Similar effects found in different dipolar solids

We performed the same pulse sequences in many different dipolar solids to show that the effects reported in Sec. III are universal. Table I summarizes the samples used in these studies and outlines dramatically different features including the T_1, which varies from 4.8 s to 5.5 h at room temperature.[20,21] Measurements in a variety of silicon samples with different doping concentrations, different dopant atoms, and even different dopant types (N type and P type) show the same qualitative results despite the significant differences in their local environments.

We also performed the same NMR pulse sequences on different nuclei.[20] The CPMG echo trains of ^{13}C in C_{60} have long tails that outlast both the measured Hahn echoes and the predicted decay when calculated by using the Ising model and delta-function π pulses. Furthermore, we see the same qualitative results for ^{89}Y in Y_2O_3. Because the natural abundance (na) of ^{89}Y is 100%, dilution of the spins on the lattice does not contribute to the results.[75,76]

Additionally, at room temperature, C_{60} molecules form an fcc lattice, and each C_{60} undergoes rapid isotropic rotation about its lattice point.[77,78] This motion eliminates any inter-C_{60} J coupling[1] but leaves the dipolar coupling between spins on different fullerenes. Thus, the J coupling, which we have not included in $\mathcal{H}_{\mathrm{int}}$ [Eq. (7)], does not play a major role in the results.[6,79]

I. Single crystal studies

In order to reduce the effects of skin depth,[30,58,59] most of our samples were ground to powder. The calculations out-

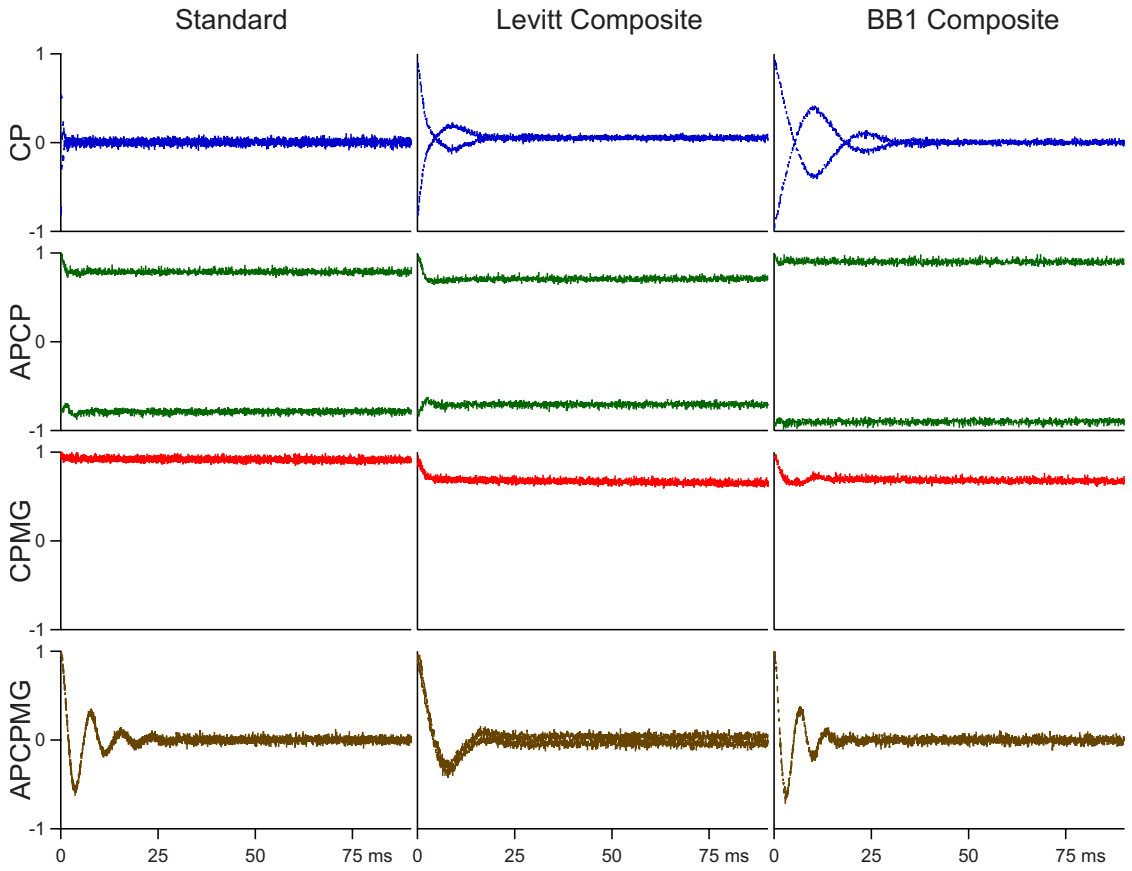

FIG. 14. (Color online) Pulse sequences CP, APCP, CPMG, and APCPMG using standard π pulses (left column), Levitt composite π pulses (middle column), and BB1 composite π pulses (right column). $H_1=35.7$ kHz, $2\tau=72$ μs, $T=300$ K, and $B^{\text{ext}}=11.74$ T.

lined in Sec. II took this into account in the disorder average by configuring each disorder realization with a random orientation of the lattice with respect to $\vec{B}^{\text{ext}}$. Then, by picking small clusters of N spins, each disorder realization was designed to represent a realistic cluster in any one powder particle.

The real ground powder particles have different shapes and sizes. Though the magnetic susceptibility of silicon is very low,[80] each powder particle would have a slightly different internal field due to its shape.[58,59] By approximating the random powder particle as an ellipsoid of revolution, we calculated the resultant magnetic susceptibility broadening of

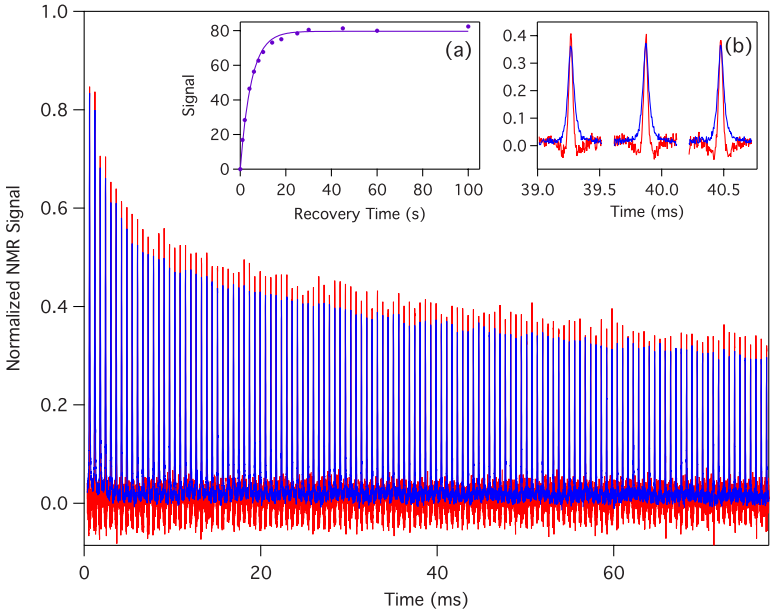

FIG. 15. (Color online) Nonequilibrium effects and spin-lattice relaxation. (Main) CPMG echo train for ^{29}Si in Si:P (3.94×10^{19} P/cm^3) with saturation-recovery times $t_{\text{rec}}=1$ s (red) and $t_{\text{rec}}=20$ s (blue). $T=300$ K, $B^{\text{ext}}=12$ T, and $2\tau=592$ μs. The initial heights of the FIDs are scaled to agree. (a) Exponential fit to the saturation-recovery experiment gives $T_1=4.9$ s in this sample. (b) Close-up of echo shapes.

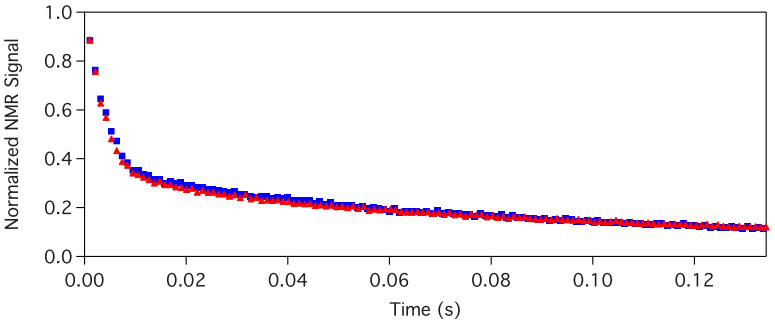

FIG. 16. (Color online) Temperature effects on CPMG tail height. CPMG echo peaks at room temperature (red) and 4 K (blue) in Si:P (3.94×10^{19} P/cm^3) diluted in paraffin wax. $2\tau = 2.192$ ms and $B^{\text{ext}} = 12$ T.

the NMR linewidth.[81–86] Convolving the magnetic susceptibility broadening with the dipolar linewidth accounted for the 290 Hz FWHM of our Si:Sb (2.75×10^{17} Sb/cm^3) powder sample.

In order to reduce the extrinsic broadening due to the magnetic susceptibility, we studied a single crystal of Si:Sb. Measurements in a single crystal allow confirmation of the lattice model and further the understanding of the magnetic susceptibility broadening. In a single crystal of Si:Sb (10^{17} Sb/cm^3), the orientation of the lattice allows only discrete coupling constants and, subsequently, a unique dipolar line shape. Additionally, the shape and orientation of the crystal with respect to $\vec{B}^{\text{ext}}$ yield a smaller spread in the internal field due to the magnetic susceptibility.[84] Figure 17 (inset, blue spectrum) plots the convolution of the dipolar line shape and the magnetic susceptibility broadening for the single crystal. The small satellites in the spectrum are due to the dipolar coupling between nearest neighbors. This simulation is a good fit to the measured spectrum [Fig. 17 (inset, red spectrum)].

In the single crystal, the CPMG echo train still exhibits a long-lived coherence for short τ [Fig. 17 (middle)] and the even-odd effect for longer τ [Fig. 17 (bottom)].

J. Magic angle spinning

The technique of magic angle spinning[1,3,4,87] (MAS) is used to reduce the dipolar coupling coefficient by rotating the entire sample about an axis tilted at 54.7° with respect to $\vec{B}^{\text{ext}}$. In the time average, the angular factor $(1-3\cos^2\theta_{jk})$ in the dipolar coupling constant [see Eq. (6)] vanishes. In addition to reducing the dipolar coupling, MAS eliminates Zeeman shift anisotropies and first-order quadrupole splittings. These experiments seek to connect $\mathcal{H}_{zz}$ to the effects outlined in Sec. III. Also, narrowing the NMR linewidth even further than in the single crystal leads to a better understanding of the population of ^{29}Si nuclei in the silicon lattice.

The FWHM of the MAS spectrum of Si:Sb (10^{17} Sb/cm^3) [Fig. 18 (top graph, red spectrum)] decreased by almost a factor of 6 compared to the spectrum of the static sample [Fig. 18 (top graph, black spectrum)]. Despite this narrowing, the MAS spectrum does not resolve distinct features in the NMR line shape. The upper limit on the spread in Zeeman shifts is consistent with the single crystal data (Fig. 17). Therefore, we conclude that only $\mathcal{H}_{\text{int}} = \mathcal{H}_Z + \mathcal{H}_{zz}$ is needed to produce the static spectrum for this sample.

Figure 18 shows the CPMG echo train for two different time delays τ taken during MAS. The top graph shows that the echo train decays even more slowly than in the static sample. Also, for very large inter-pi-pulse spacings, as shown in the bottom graph, the even-odd effect is not present. The absence of the dipolar coupling and the dramatic changes in the observed CPMG echo trains suggest that $\mathcal{H}_{zz}$ plays an important role in our static NMR studies.

We conclude this section by stating that these studies are by no means a complete study of all extrinsic effects in NMR. They are, however, representative of the high quality of the pulses that we use and the simple spin Hamiltonian of the nuclei under study. These experiments are near optimal

TABLE I. Properties of dipolar solids used in these studies. Columns display the NMR spin-1/2 nucleus, dopant concentrations in number of dopant nuclei per cm^3, gyromagnetic ratio (γ) in MHz/T, isotopic natural abundance (na) in percent, full width at half maximum of the measured spectrum (FWHM) in Hz, spin-lattice relaxation time (T_1) in seconds, and transverse relaxation time (T_2) as measured by the best exponential or Gaussian fit of the decay of Hahn echoes in milliseconds. Si:P (10^{13}) and Si:B (10^{16}) data taken at room temperature in a 7 T field (no Hahn echo data for these two samples). All other data taken at room temperature in a 12 T field.

Sample	Dopant concentration (cm^{-3})	$\gamma/2\pi$ (MHz/T)	na (%)	FWHM (Hz)	T_1 (s)	T_2 (ms)
^{13}C in C_{60}		10.7	1.11	260	25.8	14
^{29}Si in Si:P	3×10^{13}	8.46	4.67	350	17640	
^{29}Si in Si:B	1.43×10^{16}	8.46	4.67	370	10080	
^{29}Si in Si:Sb	2.75×10^{17}	8.46	4.67	200	276	6
^{29}Si in Si:P	3.43×10^{19}	8.46	4.67	3600	4.8	6
^{89}Y in Y_2O_3		2.09	100	3100	3100	24

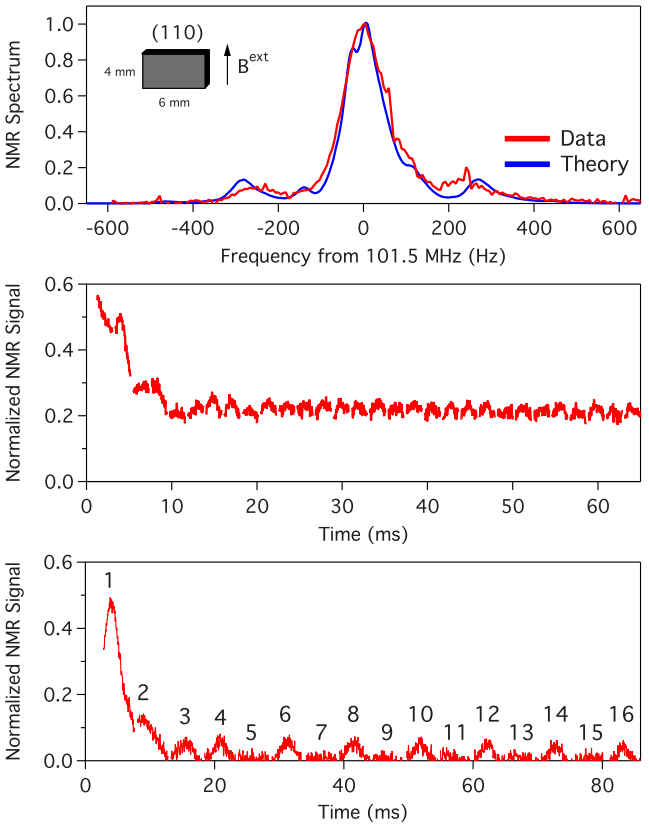

FIG. 17. (Color online) NMR data in a single crystal of Si:Sb (2.75×10^{17} Sb/cm^3) oriented with its (110) axis along $\hat{z}$ (see top inset). (Top) NMR spectrum (red) compared to a calculation for silicon that include dipolar coupling of $N=6$ spins, magnetic susceptibility broadening, and skin depth due to the crystal shape (blue). FWHM=110 Hz. (Middle) CPMG echo train for $2\tau=2.1$ ms shows the long tail. (Bottom) CPMG echo train for $2\tau=5.2$ ms shows the even-odd effect.

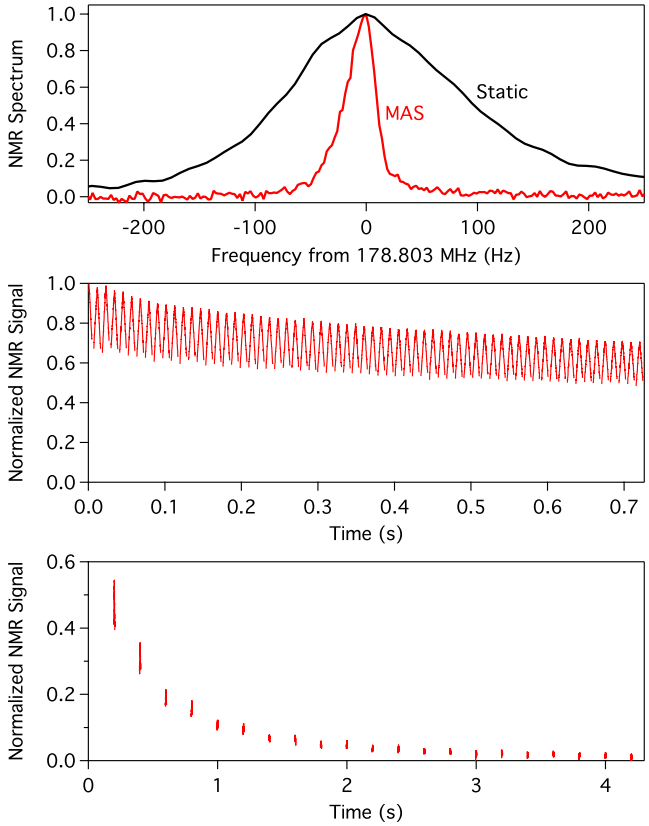

FIG. 18. (Color online) Magic angle spinning in Si:Sb (10^{17} Sb/cm^3). (Top) NMR spectrum of a static powdered sample with FWHM=175 Hz (black) and the MAS spectrum spun at 3 kHz with FWHM=31 Hz (red). (Middle) CPMG echo train while spinning. $2\tau=11.25$ ms. Long tail is expected since dipolar coupling is reduced. (Bottom) CPMG echo train while spinning. $2\tau=0.2$ s. No pronounced even-odd effect in contrast to Fig. 4 (bottom) and Fig. 17 (bottom).

yet still exhibit the unexpected behavior of multiple π pulse echo trains. From these experimental results, we can make concrete assumptions about the real pulse $\mathcal{P}$ and the real free evolution $\mathcal{V}$.

The experiments outlined in this section provide the following constraints on any theoretical model that may explain our results: (1) the relevant internal Hamiltonian should contain only the Zeeman and dipolar Hamiltonians $\mathcal{H}_{\text{int}}=\mathcal{H}_Z+\mathcal{H}_{zz}$ and (2) the pulses are strong and equally address all spins, but they are not instantaneous.

V. TREATMENT OF FINITE PULSES IN EXACT CALCULATION AND AVERAGE HAMILTONIAN THEORY

In Sec. II, we demonstrated how instantaneous π pulses allow the measurable coherence of the system to evolve as if there were no pulses applied at all. Additionally, this measurable coherence should decay to zero under the action of the dipolar Hamiltonian with time constant T_2.

However, in Sec. III, we reported experiments that contradict these expectations, such as the sensitivity of the echo train to the phase of the applied π pulses. Some of these echo trains extend well beyond the expected T_2 (CPMG, APCP), while others decay much faster (CP, APCPMG).

Additionally, the experimental explorations of Sec. IV strongly suggest that extrinsic pulse imperfections are not responsible for these large discrepancies. Our observed effects are universal across many different samples all connected by the same form of the dipolar Hamiltonian. Thus, only the Zeeman and dipolar Hamiltonians are needed but the validity of the instantaneous π pulse approximation must be reconsidered.

In this section, we calculate the exact evolution of the density matrix by numerical means. The action of strong but finite pulses under the simultaneous influence of the dipolar Hamiltonian is the intrinsic effect that can lead to the large discrepancies we have observed.

A. Exact numerical calculation with strong finite pulses

Since the delta-function pulse approximation has failed to explain our results, we return to the exact form of the pulse evolution operator from Eq. (9),

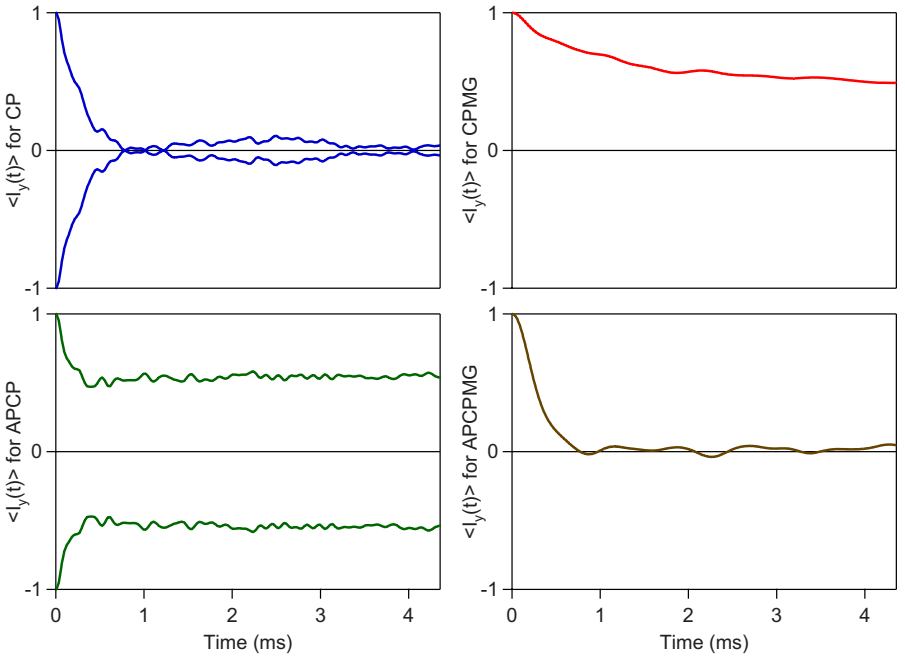

FIG. 19. (Color online) Exact calculation using strong but finite π pulses. Calculation uses the following parameters: $N=6$ spins, simulated pulse strength $H_1=40$ kHz ($t_p=12.5$ μs), delay between π pulses $2\tau=2$ μs, dipolar coupling scaled by $25\times B_{jk}$ of ^{29}Si, Zeeman shift Ω_z/h drawn from a 3 kHz wide Gaussian for each DR, and the disorder average is taken over 150 DRs. The full line shape is 4 kHz, which is a convolution of the pure dipolar line of 2.2 kHz and the Zeeman spread of 3 kHz. Compare these curves to the data of Fig. 6. CPMG and APCP display long-lived tails, while CP and APCPMG decay to zero.

$$\mathcal{P}_\phi = \exp\left[-\frac{i}{\hbar}(\mathcal{H}_Z + \mathcal{H}_{zz} + \mathcal{H}_{P_\phi})t_p\right], \tag{23}$$

where $\mathcal{H}_Z$ is the Zeeman Hamiltonian, $\mathcal{H}_{zz}$ is the secular dipolar Hamiltonian, and $\mathcal{H}_{P_\phi}=-\hbar\omega_1 I_{\phi_T}$ is the Hamiltonian form of an rf pulse applied for time t_p along the ϕ axis in the rotating frame.

To model the evolution of a spin system after n pulses, the relevant form of Eq. (1) becomes

$$\rho(t) = \{\mathcal{U}\mathcal{P}_\phi\mathcal{U}\}^n \rho(0) \{\mathcal{U}^{-1}\mathcal{P}_\phi^{-1}\mathcal{U}^{-1}\}^n, \tag{24}$$

where the free-evolution propagator is given by $\mathcal{U}=\exp[-\frac{i}{\hbar}(\mathcal{H}_Z+\mathcal{H}_{zz})\tau]$. From here, no approximations are made. Instead, numerical diagonalization is used during each $\mathcal{P}_\phi$ and $\mathcal{U}$ to evaluate $\rho(t)$ for the four pulse sequences that we consider.[20,88]

Figure 19 plots the exact calculation of $\langle I_{y_1}(t)\rangle = \mathrm{Tr}\{\rho(t)I_{y_1}\}$ [Eq. (15)] averaged over 150 disorder realizations (DRs) for the four pulse sequences CP, CPMG, APCP, and APCPMG. These exact calculations have the same qualitative trends as the experiments. Namely, CPMG and APCP produce long-lived measurable coherence, while CP and APCPMG decay away to zero. Since these exact calculations include no extrinsic imperfections, we conclude that the dipolar Hamiltonian and Zeeman Hamiltonian under the pulse must be the sole cause for the different time-evolved curves in Fig. 19.

However, there are two important caveats for these calculations. First, we used an $N=6$ spin system to simulate the behavior of a macroscopic spin system. Because of computer limitations, using a much larger system is not possible, inevitably leaving out many multi-spin entanglements. Second, to get these results using only $N=6$ spins, our simulations used both larger linewidths and shorter interpulse spacing than in the experiments. We will return to these two important points in the last part of this section to show how system size and coupling strength are related.

B. Understanding the exact calculation using average Hamiltonian theory

To understand the mechanisms underlying the exact calculation, we turn to average the Hamiltonian theory[1,3,5,45,89] to obtain approximate analytic results for the four pulse sequences under study. This analysis, in turn, allows the development of further calculations to uncover trends in the behavior of N spins under strong π pulses.

Average Hamiltonian or coherent averaging theory[89] was developed in NMR to approximate the behavior of multiple-pulse experiments that use many $\pi/2$ pulses. Additionally, the average Hamiltonian theory can be used to describe NMR experiments with very long pulses such as spin locking or the magic echo.[16,17]

Here, we wish to apply the average Hamiltonian theory to a train of strong but finite π pulses where the delta-function pulse approximation (Sec. II) predicts echoes that decay to zero. Because our pulses are so strong (Fig. 13), we expected the nonzero pulse duration to give only a small perturbation to the delta-function pulse approximation. However, the exact calculations show a dramatic departure from this expectation (Fig. 19).

The average Hamiltonian analysis starts from the total time-dependent Hamiltonian of an interacting spin system in the presence of an rf field,

$$\mathcal{H}_{\mathrm{tot}}(t) = \mathcal{H}_Z + \mathcal{H}_{zz} - \hbar\omega(t) I_{\phi_T}, \tag{25}$$

where $\omega(t)=\omega_1$ during a pulse and zero during free evolution. $\mathcal{H}_Z$ and $\mathcal{H}_{zz}$ are the Zeeman Hamiltonian and the secular dipolar Hamiltonian, respectively [Eqs. (4) and (5)]. The spin operator along ϕ can be projected along the principle

axes in the rotating frame $I_{\phi_T}=\cos\phi I_{x_T}+\sin\phi I_{y_T}$.

We label the first two terms of Eq. (25) as the internal Hamiltonian $\mathcal{H}_{\rm int}=\mathcal{H}_{zz}+\mathcal{H}_Z$ in the language of average Hamiltonian theory.[3,89] The applied pulse term then becomes the external or rf Hamiltonian $\mathcal{H}_{\rm rf}(t)=-\hbar\omega(t)I_{\phi_T}$.

The total time-evolution operator

$$U_{\rm tot}(t)=T\exp\left[-\frac{i}{\hbar}\int_0^t dt'\mathcal{H}_0(t')\right] \tag{26}$$

can then be split into a product of two parts,

$$U_{\rm tot}(t)=U_{\rm rf}(t)U_{\rm int}(t), \tag{27}$$

$$U_{\rm rf}(t)=T\exp\left[-\frac{i}{\hbar}\int_0^t dt'\mathcal{H}_{\rm rf}(t')\right], \tag{28}$$

$$U_{\rm int}(t)=T\exp\left[-\frac{i}{\hbar}\int_0^t dt'\tilde{\mathcal{H}}(t')\right], \tag{29}$$

$$\tilde{\mathcal{H}}(t)=U_{\rm rf}^{-1}(t)\mathcal{H}_{\rm int}U_{\rm rf}(t), \tag{30}$$

where T is the Dyson time-ordering operator[1] and $\tilde{\mathcal{H}}(t)$ is the toggling frame Hamiltonian.[3,5,89] This separation is convenient when $\mathcal{H}_{\rm rf}$ is periodic and cyclic with the cycle time t_c. In this case, $U_{\rm rf}(t_c)=1$ and the Magnus expansion[90] gives

$$U_{\rm int}(nt_c)=\exp\left[-\frac{i}{\hbar}nt_c(\bar{\mathcal{H}}^{(0)}+\bar{\mathcal{H}}^{(1)}+\bar{\mathcal{H}}^{(2)}+\cdots)\right], \tag{31}$$

for the time evolution after any multiple n of the cycle time. The first two terms in the expansion are given by

$$\bar{\mathcal{H}}^{(0)}=\frac{1}{t_c}\int_0^{t_c}dt\tilde{\mathcal{H}}(t), \tag{32}$$

$$\bar{\mathcal{H}}^{(1)}=-\frac{i}{2t_c\hbar}\int_0^{t_c}dt_2\int_0^{t_2}dt_1[\tilde{\mathcal{H}}(t_2),\tilde{\mathcal{H}}(t_1)]. \tag{33}$$

The advantage of the Magnus expansion is that the full time-evolution operator $U_{\rm tot}(t)$ is now written as a single exponential instead of a product of exponentials. Additionally, the terms in the average Hamiltonian expansion $\bar{\mathcal{H}}^{(0)},\bar{\mathcal{H}}^{(1)},\bar{\mathcal{H}}^{(2)}\ldots$ are time independent and exactly describe the system at multiples of the cycle time t_c. In practice, this exact expression is replaced by an approximate one when the series expansion is truncated after the first few terms.[1,3,5,45,89]

The four pulse sequences studied here all have the same cycle time $t_c=4\tau+2t_p$ consisting of two π pulses with a time delay of τ before and after each pulse. The average Hamiltonian description is simplest when the cycle time is short in the strong-pulse regime ($\hbar\omega_1\gg\Omega_z,B_{jk}$) since the expansion in Eq. (31) is then dominated by the first few terms.

By using these steps, we can calculate the leading terms for the four pulse sequences under study. For example, the time evolution of $\rho(t)$ under the CPMG sequence is

TABLE II. Toggling frame Hamiltonians $\tilde{\mathcal{H}}(t_i)$ during each event of the CPMG cycle $\{\tau-180_Y-2\tau-180_Y-\tau\}$ where t_p is the pulse time and τ is the free-evolution time. $C_\theta=\cos(\omega_1 t)$, $C_{2\theta}=\cos(2\omega_1 t)$, $S_\theta=\sin(\omega_1 t)$, and $S_{2\theta}=\sin(2\omega_1 t)$.

Event	Time	$\tilde{\mathcal{H}}(t_i)$ for CPMG
$\mathcal{U}_1$	τ	$+\Omega_z I_{z_T}+\mathcal{H}_{zz}$
$\mathcal{P}_2$	t_p	$+\Omega_z(I_{z_T}C_\theta+I_{x_T}S_\theta)-\frac{1}{2}\mathcal{H}_{yy}+\mathcal{H}_y^S C_{2\theta}+\mathcal{H}_y^A S_{2\theta}$
$\mathcal{U}_3$	2τ	$-\Omega_z I_{z_T}+\mathcal{H}_{zz}$
$\mathcal{P}_4$	t_p	$-\Omega_z(I_{z_T}C_\theta+I_{x_T}S_\theta)-\frac{1}{2}\mathcal{H}_{yy}+\mathcal{H}_y^S C_{2\theta}+\mathcal{H}_y^A S_{2\theta}$
$\mathcal{U}_5$	τ	$+\Omega_z I_{z_T}+\mathcal{H}_{zz}$

$$\rho(t)=U_{\rm tot}(t)\rho(0)U_{\rm tot}^{-1}(t)=\{\mathcal{U}_5\mathcal{P}_4\mathcal{U}_3\mathcal{P}_2\mathcal{U}_1\}^n\rho(0)\{\rm inv\}^n, \tag{34}$$

where $\mathcal{P}_2=\mathcal{P}_4$ are π pulses along $\hat{y}$ and include the Zeeman and dipolar Hamiltonians. $\mathcal{U}_i$, $i=1,3,5$ are the free-evolution propagators that only include the Zeeman and dipolar Hamiltonians.

After identifying the parts of $U_{\rm tot}$, the next step is to calculate the toggling frame Hamiltonians for each of these events. As an example, $\tilde{\mathcal{H}}(t_3)$ in CPMG for event $\mathcal{U}_3$ is

$$\begin{aligned}\tilde{\mathcal{H}}(t_3)&=\{U_{\rm rf}^{-1}(t_1)U_{\rm rf}^{-1}(t_2)U_{\rm rf}^{-1}(t_3)\}\mathcal{H}_{\rm int}\{\rm inv\}\\&=\mathcal{R}_y^{-1}(\Omega_z I_{z_T}+\mathcal{H}_{zz})\mathcal{R}_y=-\Omega_z I_{z_T}+\mathcal{H}_{zz},\end{aligned} \tag{35}$$

where the unitary operators $U_{\rm rf}$ are applied in reverse time ordering [Eq. (30)].

Table II gives the expressions for all the toggling frame Hamiltonians as modified by $\mathcal{H}_{\rm rf}$ in each event of the CPMG sequence. Note that the difference between the toggling frame transformation of the $\mathcal{U}_3$ interval and the $\mathcal{U}_1$ and $\mathcal{U}_5$ intervals is only the sign in front of the Zeeman term $\Omega_z I_{z_T}$. This detail is important because it is an explicit indication that the pulses are free from any extrinsic errors. Thus, I_z rotates to $-I_z$ after each π pulse. This rotation flips the sign of the single-spin Zeeman Hamiltonian but does nothing to the bilinear dipole Hamiltonian.

For comparison, the toggling Hamiltonians for the APCP sequence are provided in Table III. The other two sequences can be obtained with a proper sign change from the toggling Hamiltonians for CPMG and APCPMG. The toggling frame Hamiltonians for APCPMG differs from CPMG by the signs

TABLE III. Toggling frame Hamiltonians $\tilde{\mathcal{H}}(t_i)$ during each event of the APCP cycle $\{\tau-180_{\bar{X}}-2\tau-180_X-\tau\}$.

Event	Time	$\tilde{\mathcal{H}}(t_i)$ for APCP
$\mathcal{U}_1$	τ	$+\Omega_z I_{z_T}+\mathcal{H}_{zz}$
$\mathcal{P}_2$	t_p	$+\Omega_z(I_{z_T}C_\theta+I_{y_T}S_\theta)-\frac{1}{2}\mathcal{H}_{xx}+\mathcal{H}_x^S C_{2\theta}+\mathcal{H}_x^A S_{2\theta}$
$\mathcal{U}_3$	2τ	$-\Omega_z I_{z_T}+\mathcal{H}_{zz}$
$\mathcal{P}_4$	t_p	$-\Omega_z(I_{z_T}C_\theta-I_{y_T}S_\theta)-\frac{1}{2}\mathcal{H}_{xx}+\mathcal{H}_x^S C_{2\theta}-\mathcal{H}_x^A S_{2\theta}$
$\mathcal{U}_5$	τ	$+\Omega_z I_{z_T}+\mathcal{H}_{zz}$

of S_θ and $S_{2\theta}$ in event $\mathcal{P}_2$ of Table II. Similarly, CP differs from APCP also by the signs of S_θ and $S_{2\theta}$ in event $\mathcal{P}_2$ of Table III.

The time-dependent terms of the toggling frame Hamiltonians during the pulses are of key interest in this analysis. The cosine and sine terms directly depend on the strength of the rf field ω_1. It is tempting to assume the limit $\omega_1 \to \infty$ and $t_p \to 0$, which would make these time-dependent terms under the pulses negligible. After all, most experiments in this study are conducted by using very strong pulses. However, by keeping these small terms, we find that they have a large impact over many pulses.

The toggling frame Hamiltonians from Table II are fed into Eq. (32) to yield the leading order behavior for the CPMG sequence.[20] This approach is repeated for all four pulse sequences giving the zeroth-order average Hamiltonians

$$\bar{\mathcal{H}}^{(0)}_{\mathrm{CP}} = \frac{1}{t_c}(4\tau\mathcal{H}_{zz} - t_p\mathcal{H}_{xx}), \tag{36}$$

$$\bar{\mathcal{H}}^{(0)}_{\mathrm{CPMG}} = \frac{1}{t_c}(4\tau\mathcal{H}_{zz} - t_p\mathcal{H}_{yy}), \tag{37}$$

$$\bar{\mathcal{H}}^{(0)}_{\mathrm{APCP}} = \frac{1}{t_c}\left(4\tau\mathcal{H}_{zz} - t_p\mathcal{H}_{xx} + \frac{4\Omega_z t_p}{\pi} I_{y_T}\right), \tag{38}$$

$$\bar{\mathcal{H}}^{(0)}_{\mathrm{APCPMG}} = \frac{1}{t_c}\left(4\tau\mathcal{H}_{zz} - t_p\mathcal{H}_{yy} - \frac{4\Omega_z t_p}{\pi} I_{x_T}\right), \tag{39}$$

with the following first-order corrections:

$$\bar{\mathcal{H}}^{(1)}_{\mathrm{CP}} = \frac{+i}{2t_c\hbar}\frac{t_p}{\pi}(t_p[\mathcal{H}^A_x, \mathcal{H}^S_x + \mathcal{H}_{xx}] + (8\tau + 2t_p)[\Omega_z I_{y_T}, \Omega_z I_{z_T} + \mathcal{H}_{xx}]), \tag{40}$$

$$\bar{\mathcal{H}}^{(1)}_{\mathrm{CPMG}} = \frac{-i}{2t_c\hbar}\frac{t_p}{\pi}(t_p[\mathcal{H}^A_y, \mathcal{H}^S_y + \mathcal{H}_{yy}] + (8\tau + 2t_p)[\Omega_z I_{x_T}, \Omega_z I_{z_T} + \mathcal{H}_{yy}]), \tag{41}$$

$$\bar{\mathcal{H}}^{(1)}_{\mathrm{APCP}} = 0, \tag{42}$$

$$\bar{\mathcal{H}}^{(1)}_{\mathrm{APCPMG}} = 0, \tag{43}$$

where we define

$$\mathcal{H}_{xx} = \sum_{j=1}^{N}\sum_{k>j}^{N} B_{jk}(3I_{x_j}I_{x_k} - \vec{I}_j \cdot \vec{I}_k), \tag{44}$$

$$\mathcal{H}_{yy} = \sum_{j=1}^{N}\sum_{k>j}^{N} B_{jk}(3I_{y_j}I_{y_k} - \vec{I}_j \cdot \vec{I}_k), \tag{45}$$

$$\mathcal{H}^A_x = \frac{3}{2}\sum_{j=1}^{N}\sum_{k>j}^{N} B_{jk}(I_{y_j}I_{z_k} + I_{z_j}I_{y_k}), \tag{46}$$

$$\mathcal{H}^A_y = \frac{3}{2}\sum_{j=1}^{N}\sum_{k>j}^{N} B_{jk}(I_{x_j}I_{z_k} + I_{z_j}I_{x_k}), \tag{47}$$

$$\mathcal{H}^S_x = \frac{3}{2}\sum_{j=1}^{N}\sum_{k>j}^{N} B_{jk}(I_{z_j}I_{z_k} - I_{y_j}I_{y_k}), \tag{48}$$

$$\mathcal{H}^S_y = \frac{3}{2}\sum_{j=1}^{N}\sum_{k>j}^{N} B_{jk}(I_{z_j}I_{z_k} - I_{x_j}I_{x_k}). \tag{49}$$

Inspection of these expressions leads to several important conclusions. First, the average Hamiltonian expressions for all four pulse sequences reduce to the bare dipolar Hamiltonian $\mathcal{H}_{zz}$ in the limit when $t_p \to 0$. The first-order correction terms $\bar{\mathcal{H}}^{(1)}$ vanish in this limit since they are all proportional to t_p. While the instantaneous pulse approximation leads to an identical decay for all four pulse sequences, real pulses introduce dynamics unique to each sequence.

Second, all the first-order correction terms $\bar{\mathcal{H}}^{(1)}$ are strictly due to the commonly neglected time-dependent terms under the pulse. Though the prefactor is small, these first-order terms provide important contributions to the time evolution of quantum coherences.

Third, by symmetry, the alternating phase sequences APCP and APCPMG have no odd-order average Hamiltonian terms. Some sequences were designed to exploit such symmetries in an effort to eliminate the first few average Hamiltonian terms and thus reduce decay. However, in experiments and in simulations, we observe a long-lived coherence in the APCP sequence but a fast decay in the APCPMG sequence.

Fourth, changing $(+I_{x_j}, +I_{y_j}) \to (+I_{y_j}, -I_{x_j})$ maps the average Hamiltonian expressions for CP (APCP) into those for CPMG (APCPMG). Also, for $\Omega_z = 0$, $\bar{\mathcal{H}}^{(0)}_{\mathrm{CP}} \equiv \bar{\mathcal{H}}^{(0)}_{\mathrm{APCP}}$ and $\bar{\mathcal{H}}^{(0)}_{\mathrm{CPMG}} \equiv \bar{\mathcal{H}}^{(0)}_{\mathrm{APCPMG}}$ leaving only a difference in the first-order correction terms. Despite these similarities, all four pulse sequences produce very different results in experiments (Fig. 6) and in simulations (Fig. 19).

Fifth, changing $(+I_{x_j}, +I_{y_j}) \to (-I_{x_j}, -I_{y_j})$ maps Eqs. (36)–(43) into the expressions for the phase-reversed partner of each sequence. For example, if "flip CP" uses $(\bar{X}, \bar{X})$ pulses, then $\bar{\mathcal{H}}^{(0)}_{\mathrm{flipCP}} = +\bar{\mathcal{H}}^{(0)}_{\mathrm{CP}}$, while $\bar{\mathcal{H}}^{(1)}_{\mathrm{flipCP}} = -\bar{\mathcal{H}}^{(0)}_{\mathrm{CP}}$. As another example, if "flip APCP" uses $(X, \bar{X})$ pulses, then $\bar{\mathcal{H}}^{(0)}_{\mathrm{flipAPCP}} = \frac{1}{t_c}(4\tau\mathcal{H}_{zz} - t_p\mathcal{H}_{xx} - \frac{4\Omega_z t_p}{\pi} I_{y_T})$ [compare with Eq. (38)] while $\bar{\mathcal{H}}^{(1)}_{\mathrm{flipAPCP}} = \bar{\mathcal{H}}^{(1)}_{\mathrm{APCP}} = 0$.

Sixth and finally, the alternating phase sequences APCP and APCPMG have another distinct difference from CP and CPMG at the level of $\mathcal{H}^{(0)}$. In Eqs. (38) and (39), a single-spin operator appears that is proportional to both the Zeeman shift Ω_z and the pulse duration t_p.

C. Second averaging

Though the average Hamiltonian expressions [Eqs. (36)–(43)] are all different, it is not obvious how they produce the very distinct expectation values $\langle I_y(t) \rangle$ in Fig. 19. In

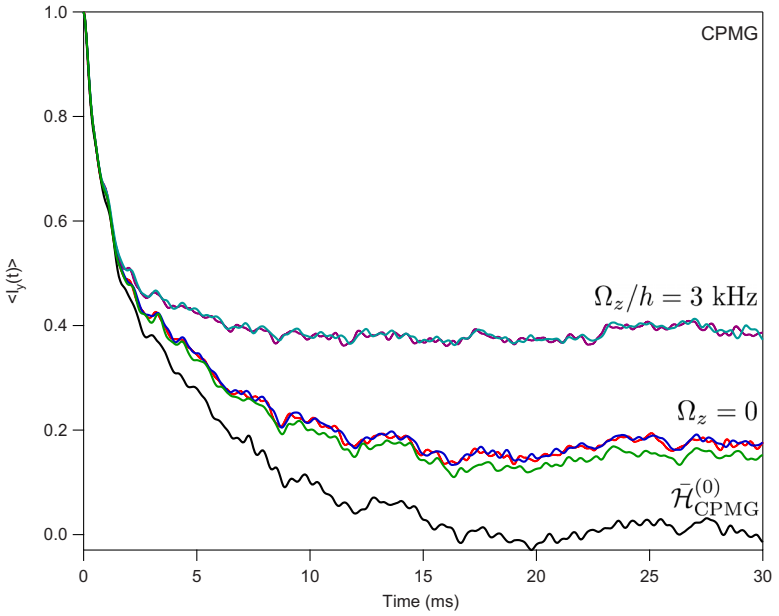

FIG. 20. (Color online) Calculations for the CPMG pulse sequence with $N=4$, $2\tau=2$ μs, $t_p=12.5$ μs, $25\times B_{jk}$ of ^{29}Si in silicon, and an average over 400 DRs. Exact calculations with Ω_z/h drawn from a 3 kHz wide Gaussian for each DR (purple curve) and $\Omega_z=0$ (red curve). Average Hamiltonian calculations $\bar{\mathcal{H}}^{(0)}_{\mathrm{CPMG}}+\bar{\mathcal{H}}^{(1)}_{\mathrm{CPMG}}$ with Ω_z/h drawn from a 3 kHz wide Gaussian for each DR (teal curve) and $\Omega_z=0$ (blue curve). Approximate calculation with $\bar{\mathcal{H}}^{(0)}_{\mathrm{CPMG}}+\bar{\mathcal{F}}^{(1)}_{\mathrm{CPMG}}$ for $\Omega_z=0$ (green curve). Zeroth-order average Hamiltonian $\bar{\mathcal{H}}^{(0)}_{\mathrm{CPMG}}$ (black curve).

order to gain insight into the mechanisms that produce these results, we rewrite the average Hamiltonian expressions by using second averaging.[3,91,92]

Equations (38) and (39) each contain a single-spin operator term (e.g., $\frac{4\Omega_z t_p}{\pi} I_{y_T}$ in $\bar{\mathcal{H}}^{(0)}_{\mathrm{APCP}}$) that looks like a transverse field coupled to the spins. Since $\bar{\mathcal{H}}^{(0)}$ is time independent, we treat this effective transverse field as a continuous field $\bar{\mathcal{H}}_{\mathrm{rf}}$ even though it only originates from the pulses. Applying average Hamiltonian theory in this second toggling frame yields

$$\bar{\bar{\mathcal{H}}}^{(0)}_{\mathrm{APCP}} = -\frac{1}{t_c}\left(2\tau - \frac{t_p}{2}\right)\mathcal{H}_{yy}, \tag{50}$$

$$\bar{\bar{\mathcal{H}}}^{(0)}_{\mathrm{APCPMG}} = -\frac{1}{t_c}\left(2\tau - \frac{t_p}{2}\right)\mathcal{H}_{xx}. \tag{51}$$

These leading order second-averaged Hamiltonians differ only in the direction of a single anisotropic dipolar Hamiltonian term. The directions for both $\mathcal{H}_{xx}$ and $\mathcal{H}_{yy}$ were dictated by the effective transverse field $\bar{\mathcal{H}}_{\mathrm{rf}}$. The effect that these anisotropic dipolar Hamiltonians have on the measurable coherence depends on the initial density matrix. For this paper, we set $\rho(0)=I_{y_T}$. From the commutation relations, we note that $\bar{\bar{\mathcal{H}}}^{(0)}_{\mathrm{APCP}}$ preserves I_{y_T} since $[I_{y_T},\mathcal{H}_{yy}]=0$, while $\bar{\bar{\mathcal{H}}}^{(0)}_{\mathrm{APCPMG}}$ does not since $[I_{y_T},\mathcal{H}_{xx}]\neq 0$. Therefore, this second-averaging analysis predicts that APCP will have long-lived coherence, while APCPMG should rapidly decay toward zero.

However, only considering Eqs. (50) and (51) would be a mistake since higher order corrections in this second-averaged Magnus expansion are non-negligible. Strictly truncating the second-averaged Hamiltonian to Eqs. (50) and (51) is only a good approximation when $\Omega_z t_p \gg B_{jk} t_c$. In contrast, our experiments are typically in the regime where $\Omega_z t_p$ is comparable to $B_{jk} t_c$. Still, our experimental results show long-lived coherence in APCP, suggesting that the higher-order corrections do not induce decay.

Because a similar difference exists between the CP and CPMG pulse sequences, we wish to apply the idea of second averaging to their average Hamiltonian expressions as well. However, because Eqs. (36) and (37) do not have similar effective transverse fields, we must look to their first-order correction terms.

For CPMG, the first-order term $\bar{H}^{(1)}_{\mathrm{CPMG}}$[Eq. (41)] contains a single-spin operator proportional to $\Omega_z^2 I_{y_T}$ from the commutator $[I_{x_T},I_{z_T}]$. Similarly, $\bar{H}^{(1)}_{\mathrm{CP}}$ [Eq. (40)] contains a term proportional to $\Omega_z^2 I_{x_T}$. These single-spin terms are analogous to the effective transverse fields that produced $\bar{\bar{H}}^{(0)}_{\mathrm{APCP}}$ and $\bar{\bar{H}}^{(0)}_{\mathrm{APCPMG}}$. Thus, this analysis predicts long-lived coherence in CPMG and a fast decay in CP, at least for large Ω_z (Fig. 19).

However, in experiments, we observed a long tail in CPMG even for very small Ω_z. This experimental result inspired us to re-examine $\bar{H}^{(1)}_{\mathrm{CPMG}}$ for another single-spin operator. Evaluating Eq. (41) for $\Omega_z=0$ gives

$$\bar{\mathcal{H}}^{(1)}_{\mathrm{CPMG}}|_{\Omega_z=0} = \frac{-i}{2t_c\hbar}\frac{t_p^2}{\pi}[\mathcal{H}_y^A,\mathcal{H}_y^S+\mathcal{H}_{yy}]. \tag{52}$$

There are many multispin operators in this expression but the only single-spin operator left in Eq. (52) is

$$\bar{\mathcal{F}}^{(1)}_{\mathrm{CPMG}} \equiv -\frac{9t_p^2}{16\pi t_c\hbar}\sum_{j=1}^{N}\sum_{k>j}^{N} B_{jk}^2(I_{y_j}+I_{y_k}). \tag{53}$$

Although this term is indeed a single-spin operator, it is not proportional to the total spin operator I_{y_T}. Nevertheless, the effect of $\bar{\mathcal{F}}^{(1)}_{\mathrm{CPMG}}$ on $\bar{\mathcal{H}}^{(0)}_{\mathrm{CPMG}}$ can be examined by calculating the time evolution of $\langle I_{y_1}(t)\rangle$ using only $\bar{\mathcal{H}}^{(0)}_{\mathrm{CPMG}}+\bar{\mathcal{F}}^{(1)}_{\mathrm{CPMG}}$ [Fig. 20 (green curve)].

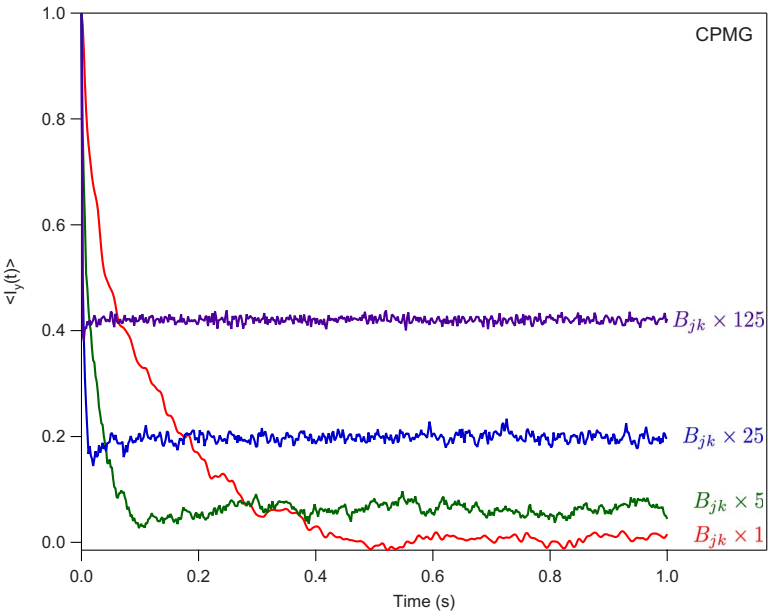

FIG. 21. (Color online) Calculations of the time evolution of $\langle I_y(t)\rangle$ under $\bar{\mathcal{H}}^{(0)}_{\mathrm{CPMG}}+\bar{\mathcal{H}}^{(1)}_{\mathrm{CPMG}}$ [Eqs. (37) and (41)] with different coupling strengths as multiples of B_{jk} for ^{29}Si in silicon ($B_{jk}\times 1$ produces a dipolar linewidth of 90 Hz). Parameters: $N=4$ spins, $\Omega_z=0$, $H_1=40$ kHz, $2\tau=2$ μs, and 1000 DR average. Exact calculations produce similar curves for these parameters.

For comparison, Fig. 20 plots exact calculations and average Hamiltonian calculations for the CPMG sequence. Without any additions, $\bar{H}^{(0)}_{\mathrm{CPMG}}$ [Fig. 20 (black curve)] decays to zero. Using the average Hamiltonian $\bar{\mathcal{H}}^{(0)}_{\mathrm{CPMG}}+\bar{\mathcal{H}}^{(1)}_{\mathrm{CPMG}}$ to time evolve the expectation value $\langle I_y(t)\rangle$ yields a long tail in good agreement with the exact calculation for the case where Ω_z/h is drawn from a 3 kHz wide Gaussian for each DR [Fig. 20 (teal curve compared to purple curve)].

Even for the case of $\Omega_z=0$, the average Hamiltonian $\bar{\mathcal{H}}^{(0)}_{\mathrm{CPMG}}+\bar{\mathcal{H}}^{(1)}_{\mathrm{CPMG}}$ [Fig. 20 (blue)] is still in good agreement with the exact calculation [Fig. 20 (red)]. These curves show that the long tail in CPMG can exist in the absence of the $\Omega_z^2 I_{y_T}$ term. Surprisingly, we also find that $\bar{\mathcal{H}}^{(0)}_{\mathrm{CPMG}}+\bar{\mathcal{F}}^{(1)}_{\mathrm{CPMG}}$ [Fig. 20 (green curve)] fits together with these two curves despite the terms that were neglected. However, these neglected terms also contribute to a tail in calculations of $\bar{H}^{(0)}_{\mathrm{CPMG}}+\bar{H}^{(1)}_{\mathrm{CPMG}}-\bar{F}^{(1)}_{\mathrm{CPMG}}$. Furthermore, multispin terms play an even bigger role in systems with stronger coupling or a larger number of spins.

The emphasis of this section was to highlight the influence of a few important terms in the average Hamiltonian [Eqs. (36)–(43)]. Focusing on only a few terms allows us to understand the qualitative results in calculations of $\langle I_{y_1}(t)\rangle$. The exact calculation contains more physics. As we shall show in Sec. VI, the qualitative similarities pointed out in the second averaging of APCP and CPMG, for example, do not give a complete picture of the evolution of $\rho(t)$ (Fig. 25).

D. Reconciling simulations with experiments

We now address the two important caveats that we made for the exact calculations of Fig. 19. Namely, we included only a small number of spins in our exact calculation and

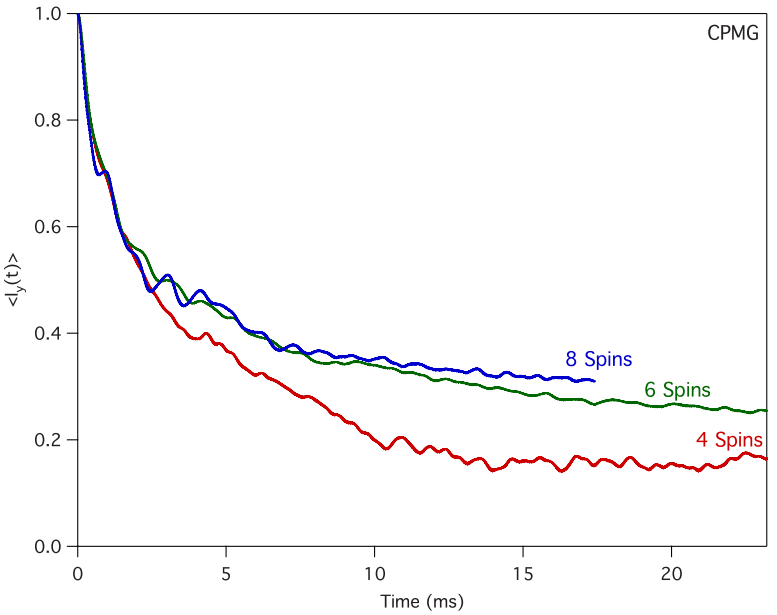

FIG. 22. (Color online) Exact calculations of the CPMG pulse sequence show that the tail height of the measurable coherence increases with system size [even N are compared to avoid artifacts (Ref. 93)]. Parameters: $\Omega_z=0$, $H_1=40$ kHz, $2\tau=2$ μs, $25\times B_{jk}$ of ^{29}Si in silicon with a dipolar linewidth of 2.2 kHz, and 400 DR average (100 DR average for $N=8$).

TABLE IV. Trace norms of the N-spin pure rf pulse Hamiltonian, $\mathcal{H}_{P_Y}=-\hbar\omega_1 I_{y_T}$, compared to that of the internal dipolar Hamiltonian $\mathcal{H}_{zz}$. The local energy scale per spin is calculated by dividing the total energy norms by $\|I_{z_T}\|=\sqrt{N2^{N-2}}$. Calculations were made by using Fig. 22 parameters: $\Omega_z=0$, $25\times B_{jk}$ of ^{29}Si in silicon, $H_1=40$ kHz, and averaged over 400 disorder realizations. Values are given in kHz.

Expression	$N=4$	$N=6$	$N=8$
	Total trace norms		
$\|\mathcal{H}_{P_Y}\|/h$	160.0	391.9	905.1
$\|\mathcal{H}_{zz}\|/h$	4.1	10.2	25.9
	Trace norms per spin		
$(\|\mathcal{H}_{P_Y}\|/\|I_{z_T}\|)/h$	40.0	40.0	40.0
$(\|\mathcal{H}_{zz}\|/\|I_{z_T}\|)/h$	1.0	1.0	1.1

inflated the dipolar coupling strength slightly above the experimental values in order to accentuate the contributions of the time-dependent terms under the pulses. For simplicity, this discussion considers only the CPMG pulse sequence with $\Omega_z=0$.

Figure 21 shows a set of calculations of $\langle I_y(t)\rangle$ evolved under the first two terms of the Magnus expansion for the CPMG sequence $(\bar{H}^{(0)}_{\mathrm{CPMG}}+\bar{H}^{(1)}_{\mathrm{CPMG}})$ for different dipolar coupling strengths. For weak dipolar coupling strengths ($B_{jk}\times 1$ of ^{29}Si in silicon), the measured coherence decays to zero in agreement with the delta-function pulse approximation (see Sec. II). As B_{jk} increases, the initial decay rate increases, which is consistent with the dipolar linewidth.[1,2,40,41,43] For large B_{jk}, this initial decay is followed by a long tail that increases with dipolar coupling strength.

Figure 22 shows a different set of calculations where the CPMG tail height increases with system size. In this case, the coupling strength is fixed at 25 times that of ^{29}Si, while each exact calculation considers a different number of spins N. By keeping B_{jk} fixed, the initial decay is very similar for the three system sizes shown. However, after some time, the effect of many strong but finite π pulses appears to produce a long-lived tail in the measured coherence that depends on N.

The system size dependence of the CPMG tail height in Fig. 22 is peculiar and deserves further analysis. In Table IV, we report our simulated numerical values of the size of both the external rf pulse Hamiltonian, $\mathcal{H}_{P_Y}=-\hbar\omega_1 I_{y_T}$, and the internal dipolar Hamiltonian, $\mathcal{H}_{\mathrm{int}}=\mathcal{H}_{zz}$, by using the trace norm[3,45,89] where $\|A\|=\sqrt{\mathrm{Tr}\{A^\dagger A\}}$. On a per-spin basis, the rf pulse is ~40 times the size of the dipolar Hamiltonian, well into the strong-pulse regime. Therefore, the deviation from the delta-function pulse limit should be tiny for any single pulse. Moreover, there is no N dependence in the per-spin comparison of energy scales, which is consistent with the nearly identical initial decays of all three curves in Fig. 22. On the other hand, the tail height at later times in Fig. 22 is N dependent; the total internal energy scale $\|\mathcal{H}_{zz}\|$ in Table IV is also N dependent.

Since the CPMG tail height is sensitive to both the dipolar coupling strength and the system size, we performed a comparative calculation in an attempt to extrapolate the results of Fig. 19 toward a system with large N and weak B_{jk} (as in silicon). Figure 23 shows a pair of calculations where N is increased while B_{jk} is decreased. The $N=4$ spin calculation uses a dipolar coupling strength 25 times stronger than that of silicon, while the $N=6$ spin calculation uses a reduced dipolar coupling strength of $25/\sqrt{6}$ times that of silicon. We reduced the dipolar coupling strength by the ratio of the system sizes by using the trace norm scaling[3,45,89] $\|I_{z_T}\|=\sqrt{\mathrm{Tr}\{I_{z_T}^2\}}=\sqrt{N2^{(N-2)}}$ in order to keep $\|\mathcal{H}_{zz}\|$ constant between the two calculations. The relative agreement in the calculated CPMG tail height supports the notion that small systems of strongly coupled spins share similarities with large systems of weakly coupled spins.

These scaling calculations show that the total dipolar energy of the system, which increases with system size, is an

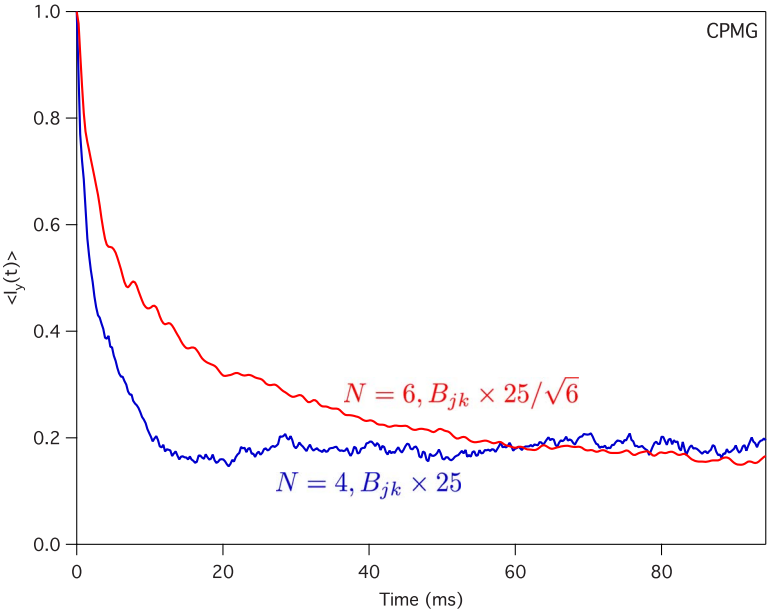

FIG. 23. (Color online) Exact calculations changing both dipolar coupling strength and system size. By adding more spins, the dipolar coupling strength can be reduced to yield a similar tail height in CPMG. Parameters: $\Omega_z=0$, $H_1=40$ kHz, $2\tau=2$ μs, and 400 DR average.

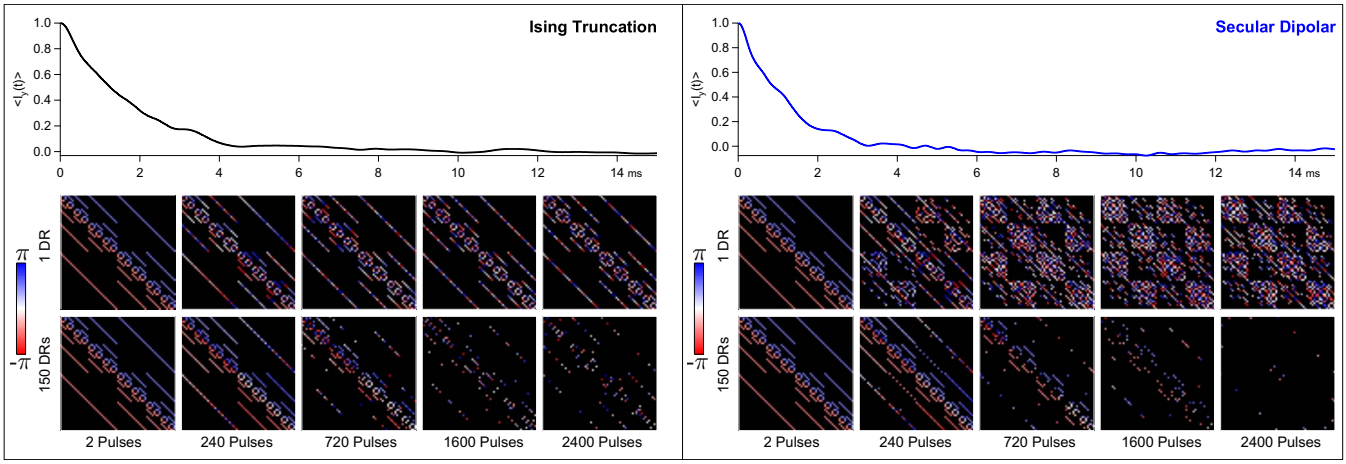

FIG. 24. (Color online) Dipolar decay of $\langle I_{y_1}(t)\rangle$ with snapshots of the z-basis density matrix evolving in time under the Ising Hamiltonian (left) and the secular dipolar Hamiltonian (right). Parameters: $N=6$, $\rho(0)=I_{y_T}$, $\Omega_z=0$, $H_1=40$ kHz, $2\tau=2\mu$s, $25\times B_{jk}$ of ^{29}Si in silicon, and $B_{jk}=0$ during pulses. The phase is colored on a red-white-blue color scale (inset). Cells are set to black if their magnitude is less than $1/10$ of the largest initially filled cells. In a single DR, the initial phase coherence is lost after many pulses by using $\mathcal{H}_{\text{Ising}}$ (left). Using $\mathcal{H}_{zz}$ (right) spreads coherence to other parts of the density matrix and mixes their phase. After an average over 150 DRs, the initial state has decayed in both cases (Ref. 95).

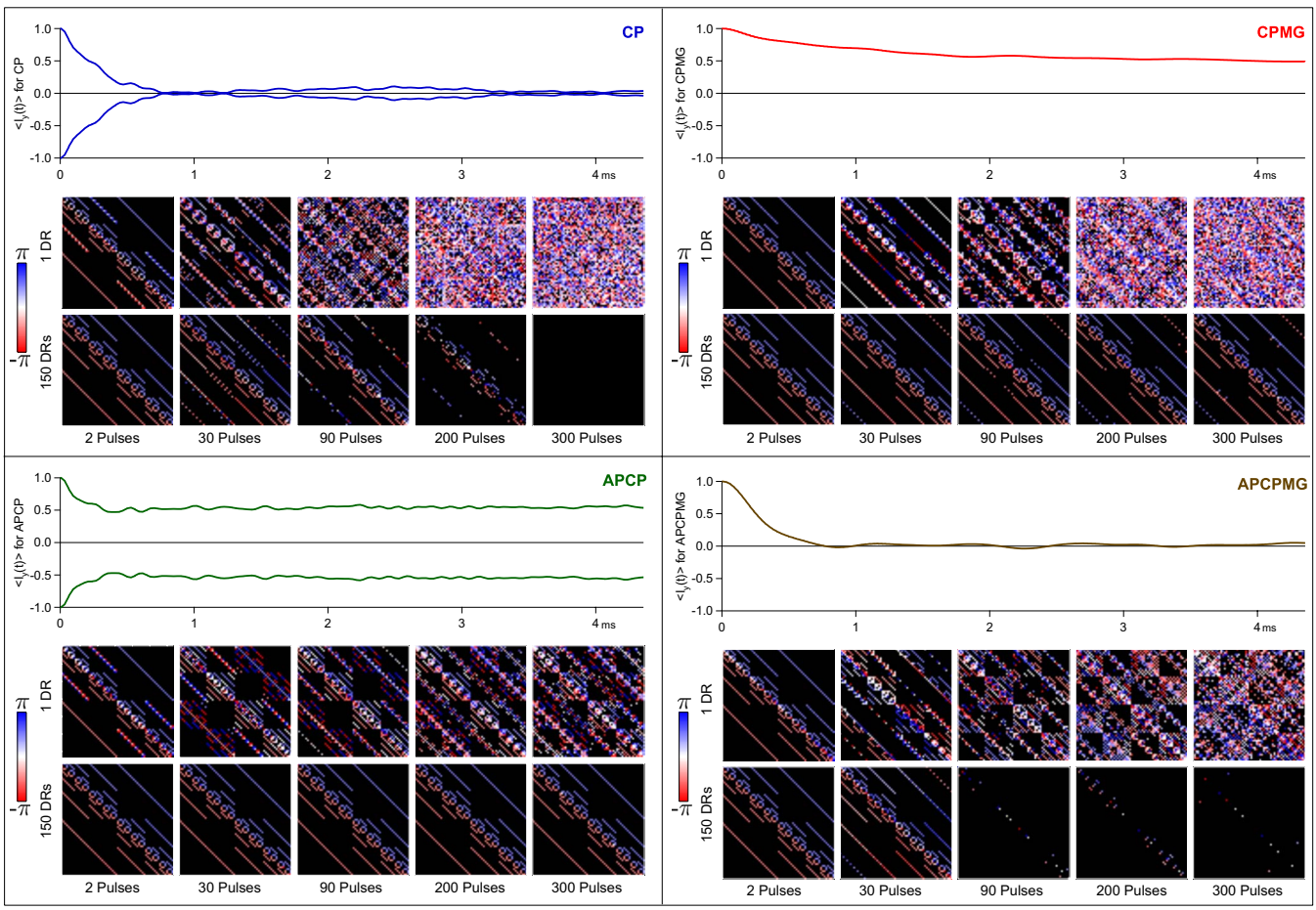

FIG. 25. (Color online) Expectation value $\langle I_{y_1}(t)\rangle$ and the density matrix $\rho(t)$ as they evolve under four different pulse sequences with $N=6$, Ω_z/h drawn from a 3 kHz wide Gaussian, $25\times B_{jk}$ of ^{29}Si in silicon, $H_1=40$ kHz, and $2\tau=2$ μs. The phase is colored on a red-white-blue color scale (inset). Cells with negligible magnitude are colored black. Compare the single DR density matrix snapshots with those of Fig. 24. Much more coherence is spread about the density matrix in these exact calculations; yet, the disorder average can yield long-lived coherence (CPMG and APCP) as well as fast decay (CP and APCPMG). (Ref. 95).

important parameter in finite π pulse effects. It is unknown whether a saturation would occur at some large N or how strong the pulses need to be in a real system so that the delta-function pulse approximation can safely be invoked.

VI. VISUALIZING THE DYNAMIC DENSITY MATRIX: EFFECTS OF EXTRA QUANTUM COHERENCE TRANSFER PATHWAYS

The multiple-pulse experiments and calculations presented thus far have been concerned with the disorder-averaged expectation value $\langle I_{y_1}(t)\rangle = \mathrm{Tr}\{\rho(t) I_{y_1}\}$. We can gain more insight into the full quantum dynamics of the spin system by visualizing the time evolution of $\rho(t)$, both for a single DR and for an average over many DRs.

For an $N=6$ spin system, $\rho(t)$ is a $2^6 \times 2^6$ matrix[1,4] of complex numbers $z=re^{i\theta}$ that is difficult to present in compact form. Since the initial state of the system following the 90_X pulse is $\rho(0)=I_{y_T}$, we found it convenient to visualize the state of $\rho(t)$ by using a red-white-blue color scale to represent the phase angle θ of each cell in $\rho(t)$. Any cells that have magnitudes $r<1/10$ of the largest initial magnitudes are colored black.

We start with the calculation for the case of CPMG with delta-function π pulses as we have outlined in Sec. II. By setting the Zeeman spread $\Omega_z=0$, the evolution of $\rho(t)$ is caused by the dipolar Hamiltonian alone.

Figure 24 shows the disorder-averaged expectation value $\langle I_y(t)\rangle$ for $N=6$ spins coupled by either the truncated Ising Hamiltonian [Fig. 24 (Ising)],

$$\mathcal{H}_{\mathrm{Ising}} = \sum_{j=1}^{N} \sum_{k>j}^{N} 2B_{jk} I_{z_j} I_{z_k}, \tag{54}$$

or by the secular dipolar Hamiltonian [Fig. 24 (Secular)],

$$\mathcal{H}_{zz} = \sum_{j=1}^{N} \sum_{k>j}^{N} 2B_{jk} \left[I_{z_j} I_{z_k} - \frac{1}{4}(I_j^+ I_k^- + I_j^- I_k^+) \right], \tag{55}$$

along with snapshots of the corresponding density matrix for each case.

In a single DR, the final density matrix under $\mathcal{H}_{\mathrm{Ising}}$ looks very similar to the initial density matrix; however, the phase of each nonzero element has been scrambled from its initial phase (see Fig. 24). The scrambled phase in a single DR translates to a decay of the magnitude in the average over 150 DRs and, thus, also the decay of $\langle I_{y_1}(t)\rangle$.

Figure 24 shows that the secular dipolar Hamiltonian also scrambles the phase of the density matrix as it evolves in time. In a single DR, $\mathcal{H}_{zz}$ also spreads coherence to additional cells in the density matrix. The mechanism responsible for the spreading of coherence in this case are the flip-flop terms of $\mathcal{H}_{zz}$. These terms allow the transitions between spin states that conserve z-angular momentum. Both the flip-flop terms and the initial density matrix proportional to I_{y_T} dictate the possible cells that can be reached after time evolution.[1,4,41] Through both the scrambling of the phase and the spread of coherence, the evolution of the density matrix for delta-function pulses leads to a decay in the disorder average.

For finite pulses, the evolution of the density matrix can be very different. Figure 25 shows the density matrix as it evolves under the four pulse sequences

$$\mathrm{CP}: 90_X - \tau - \{180_X - 2\tau - 180_X - 2\tau\}^n,$$

$$\mathrm{APCP}: 90_X - \tau - \{180_{\bar{X}} - 2\tau - 180_X - 2\tau\}^n,$$

$$\mathrm{CPMG}: 90_X - \tau - \{180_Y - 2\tau - 180_Y - 2\tau\}^n,$$

$$\mathrm{APCPMG}: 90_X - \tau - \{180_{\bar{Y}} - 2\tau - 180_Y - 2\tau\}^n,$$

where the internal Hamiltonian is present during the strong but finite pulses. Note that even after the first two π pulses, $\rho(t)$ looks very similar to $\rho(0)$ since ω_1 is big and the difference from a pure rotation is small. Nevertheless, in contrast to the delta-function pulse approximation, these pulse sequences allow much more coherence transfer to different cells of the density matrix. In particular, for the CP and CPMG sequences, the spread of coherence has reached every single cell of the $2^6 \times 2^6$ density matrix after evolving under 300 strong but finite π pulses.

The average Hamiltonian expressions for the four pulse sequences give us a better understanding of the mechanism of coherence flow to other cells of the density matrix for the case of finite pulses. For example, the APCP sequence has a zeroth-order average Hamiltonian

$$\mathcal{H}^{(0)}_{\mathrm{APCP}} = \sum_{j=1}^{N} \sum_{k>j}^{N} B_{jk} [\kappa_1 I_{z_j} I_{z_k} + \kappa_2 (I_j^+ I_k^- + I_j^- I_k^+) + \kappa_3 (I_j^+ I_k^+ + I_j^- I_k^-)] + \kappa_4 (I_j^+ - I_j^-), \tag{56}$$

when expressed by using the raising and lowering operators. Here, $\kappa_1 = \frac{8\tau + t_p}{t_c}$, $\kappa_2 = \frac{4\tau + t_p}{4t_c}$, $\kappa_3 = -\frac{3t_p}{4t_c}$, and $\kappa_4 = -i\frac{2\Omega_z t_p}{\pi t_c}$. The last two terms in Eq. (56) do not appear in the Hamiltonian under the delta-function pulse approximation [Eq. (55)]. Furthermore, these terms are distinct because they do not conserve z-angular momentum. The appearance of these terms is yet another intrinsic property of the finite pulse. Regardless of how well real pulses are engineered to reduce t_p, unless t_p is exactly zero, these extra terms will enable the spread of coherence to parts of the density matrix fundamentally forbidden in the delta-function pulse approximation. Thus, after the application of many π pulses, the final density matrix could be nowhere near the expected result, if we fail to consider the action of real pulses.

The significance of our argument for NMR would be lost if these extra coherence transfer pathways only led to an imperceptible difference in the decay of $\langle I_{y_1}(t)\rangle$. However, as Fig. 25 shows, the enhanced spread of coherence in a single DR can surprisingly preserve the measurable coherence (CPMG and APCP) or lead to a decay (CP and APCPMG) in the disorder average depending on the phase of the π pulses. Thus, it is of considerable importance to understand the entire density matrix since real pulses connect all cells back to the measurable channel.

To illustrate the influence of these new coherence transfer pathways[4] to the measurable cells, we performed a "knock-out" calculation[88] that periodically zeros cells in the density

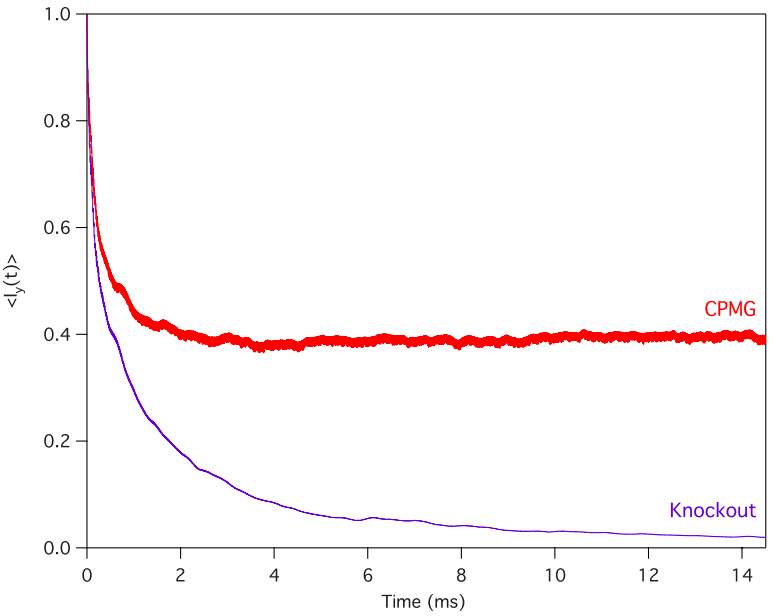

FIG. 26. (Color online) Knockout calculations for CPMG. Parameters: $N=6$, $150\times B_{jk}$ of ^{29}Si in silicon, $\Omega_z=0$, $H_1=40$ kHz, $2\tau=2$ μs, and 400 DR average. The knockout trace (purple) is calculated by deleting density matrix cells with quantum coherence order $q\neq\pm 1$ after each π pulse. (The delta-function pulse approximation assumes that all coherences stay as $q=\pm 1$ for all times.) The long tail in the exact CPMG calculation (red) requires coherence transfer pathways between all quantum coherences (Refs. 1, 4, and 88).

matrix that should always be zero under the secular dipolar Hamiltonian and delta-function π pulses [i.e., cells that remain black in Fig. 24 (secular dipolar) after 2400 pulses in 1 DR]. The red curve in Fig. 26 is the disorder-averaged $\langle I_{y_1}(t)\rangle$ for the CPMG sequence with a long-lived tail. The purple curve is the same CPMG pulse sequence but applies the knockout procedure after each π pulse and in each DR. Because of the drastic decay of the knockout curve, we infer that not only do these extra coherence transfer pathways exist but they allow coherence to constructively flow back to the measurable channel leading to the long tail in the CPMG sequence.

VII. CONCLUSIONS

We have shown experimental evidence of pulse sensitivity in dipolar solids for a variety of samples and experimental conditions. We find that the spin system is intrinsically sensitive to the phase and presence of real finite pulses even when these pulses are much stronger than the spectral linewidth. Furthermore, exact calculations show this pulse sequence sensitivity in small clusters of spins with large coupling strength and short interpulse spacing. We suggest that our findings should apply to large numbers of spins with weaker coupling and longer interpulse spacing based on a phenomenological scaling of our exact results. The results of the exact calculation and average Hamiltonian analysis show that no extrinsic effects are needed to describe the phenomena.

Conventional expectations from NMR theory suggest that the delta-function pulse approximation is applicable when the pulse is much stronger than the spread of Zeeman energies ($\hbar\omega_1 \gg \Omega_z$) and much stronger than the coupling strength ($\hbar\omega_1 \gg B_{jk}$). However, we have shown that the delta-

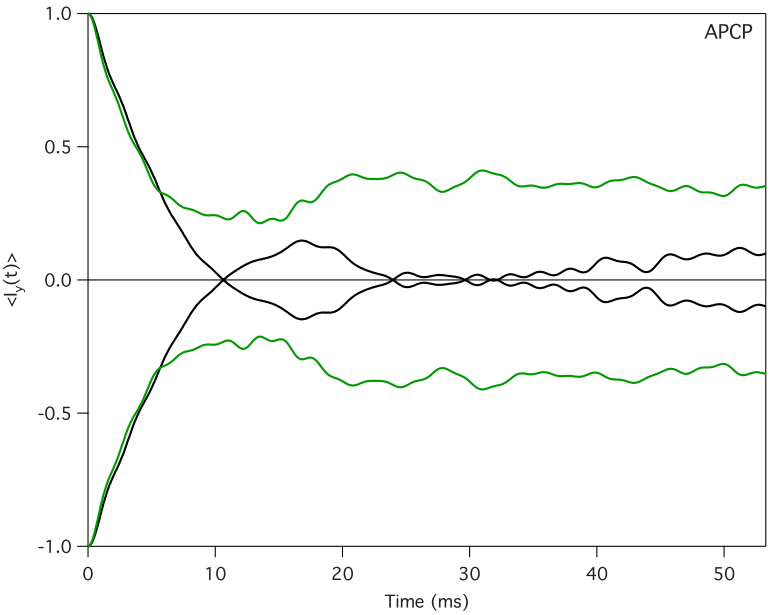

FIG. 27. (Color online) Calculations for APCP with $N=4$, Ω_z/h drawn from a 290 Hz wide Gaussian, $1\times B_{jk}$ of ^{29}Si in silicon, $H_1=1.5$ MHz, $2\tau=2$ μs, and 100 DR average. Even for $H_1/\mathrm{FWHM}=5000$, the delta-function pulse approximation (black) misses important physics from the exact calculation (green).

function pulse approximation can miss important physics for any real pulse in the presence of an always-on internal Hamiltonian. These effects are especially pronounced when considering the action of π pulses since the unique pulse-dependent terms have no analog in the delta-function pulse approximation.[20]

Simply ignoring the intrinsic effects under real finite pulses can lead to dramatic consequences, as shown in Fig. 27. The green trace shows the exact calculation of $\langle I_{y_1}(t)\rangle$ for the APCP sequence under the action of finite pulses. The black trace is the same calculation but where we have artificially set the internal Hamiltonian to zero during the pulses. It is particularly alarming to note that we have used a pulse strength that is 5000 times stronger than the full width at half maximum of the NMR spectrum; yet, the two curves do not agree. The validity of the delta-function pulse approximation needs to be justified carefully and quantitatively, at least in the limit of many spins, many π pulses, or both.

Our findings have an important connection to the field of quantum information processing since many quantum algorithms call for the application of repeated π pulses to a quantum system.[7–12] Typically, the delta-function pulse approximation is used in the analysis. While we have not considered all possible internal Hamiltonians or pulse types, we caution the reader that the validity of the delta-function pulse approximation should be checked for each system. Our results suggest that to obtain the ideal behavior of repeated π pulse sequences, the internal Hamiltonian should be completely set to zero during the action of any real pulse. It may not be enough to simply reduce the coupling strength, even by an order of magnitude. Furthermore, any effective transverse field during the pulses could also change the system's expected response after many pulses are applied. The effects of real pulses need to be taken into account if the promise of quantum control is to be realized.

More theoretical research on this problem could lead to a deeper understanding of the interplay between the internal Hamiltonian and real pulse action.[88] It should also be possible to take advantage of the dynamics under the real pulse in the development of advanced strong-pulse sequences.[94]

ACKNOWLEDGMENTS

We thank X. Wu, E. Paulson, and K. W. Zilm for their experimental assistance and C. P. Slichter, V. V. Dobrovitski, S. M. Girvin, J. D. Walls, and M. M. Maricq for helpful discussions. Silicon samples were provided by R. Falster (MEMC) and T. P. Ma. This work was supported in part by the National Security Agency (NSA) and Advanced Research and Development Activity (ARDA) under Army Research Office (ARO) Contracts No. DAAD19-01-1-0507 and No. DAAD19-02-1-0203, and by the NSF under Grants No. (FRG) DMR-0653377, No. (ITR) DMR-0325580, and No. DMR-0207539.

*sean.barrett@yale.edu
†http://opnmr.physics.yale.edu

[1] C. P. Slichter, *Principles of Magnetic Resonance*, 3rd ed. (Springer, New York, 1996).
[2] A. Abragam, *The Principles of Nuclear Magnetism*, 2nd ed. (Clarendon, Oxford, 1961).
[3] M. Mehring, *Principles of High-Resolution NMR in Solids*, 2nd ed. (Springer-Verlag, Berlin, 1983).
[4] R. R. Ernst, G. Bodenhausen, and A. Wokaun, *Principles of Nuclear Magnetic Resonance in One and Two Dimensions* (Clarendon, Oxford, 1987).
[5] U. Haeberlen, *High Resolution NMR in Solids: Selective Averaging* (Academic, New York, 1976), Vol. 1.
[6] R. Freeman, *Spin Choreography: Basic Steps in High Resolution NMR* (Spektrum, Oxford, 1997).
[7] L. Viola and S. Lloyd, Phys. Rev. A **58**, 2733 (1998).
[8] G. S. Uhrig, Phys. Rev. Lett. **98**, 100504 (2007).
[9] J. J. L. Morton, A. M. Tyryshkin, A. Ardavan, S. C. Benjamin, K. Porfyrakis, S. A. Lyon, and G. A. D. Briggs, Phys. Status Solidi B **243**, 3028 (2006).
[10] P. Cappellaro, J. S. Hodges, T. F. Havel, and D. G. Cory, J. Chem. Phys. **125**, 044514 (2006).
[11] P. Facchi, S. Tasaki, S. Pascazio, H. Nakazato, A. Tokuse, and D. A. Lidar, Phys. Rev. A **71**, 022302 (2005).
[12] L. M. K. Vandersypen and I. L. Chuang, Rev. Mod. Phys. **76**, 1037 (2004).
[13] E. D. Ostroff and J. S. Waugh, Phys. Rev. Lett. **16**, 1097 (1966).
[14] J. G. Powles and P. Mansfield, Phys. Lett. **2**, 58 (1962).
[15] P. Mansfield, J. Phys. C **4**, 1444 (1971).
[16] W. K. Rhim, A. Pines, and J. S. Waugh, Phys. Rev. Lett. **25**, 218 (1970).
[17] W. K. Rhim, A. Pines, and J. S. Waugh, Phys. Rev. B **3**, 684 (1971).
[18] W. K. Rhim, D. D. Elleman, and R. W. Vaughan, J. Chem. Phys. **58**, 1772 (1973).
[19] J. S. Waugh, L. M. Huber, and U. Haeberlen, Phys. Rev. Lett. **20**, 180 (1968).
[20] Dale Li, A. E. Dementyev, Yanqun Dong, R. G. Ramos, and S. E. Barrett, Phys. Rev. Lett. **98**, 190401 (2007).
[21] A. E. Dementyev, D. Li, K. MacLean, and S. E. Barrett, Phys. Rev. B **68**, 153302 (2003).
[22] M. B. Franzoni and P. R. Levstein, Phys. Rev. B **72**, 235410 (2005).
[23] T. D. Ladd, D. Maryenko, Y. Yamamoto, E. Abe, and K. M. Itoh, Phys. Rev. B **71**, 014401 (2005).
[24] S. A. Lyon (private communication).
[25] S. Watanabe and S. Sasaki, Jpn. J. Appl. Phys., Part 2 **42**, L1350 (2003).
[26] H. Alloul and P. Dellouve, Phys. Rev. Lett. **59**, 578 (1987).
[27] S. E. Fuller, E. M. Meintjes, and W. W. Warren, Phys. Rev. Lett. **76**, 2806 (1996).
[28] G. Lampel, Phys. Rev. Lett. **20**, 491 (1968).
[29] R. G. Shulman and B. J. Wyluda, Phys. Rev. **103**, 1127 (1956).
[30] R. K. Sundfors and D. F. Holcomb, Phys. Rev. **136**, A810 (1964).
[31] D. P. DiVincenzo and D. Loss, J. Magn. Magn. Mater. **200**, 202

(1999).
[32] B. E. Kane, Nature (London) **393**, 133 (1998).
[33] B. E. Kane, Fortschr. Phys. **48**, 1023 (2000).
[34] T. D. Ladd, J. R. Goldman, F. Yamaguchi, Y. Yamamoto, E. Abe, and K. M. Itoh, Phys. Rev. Lett. **89**, 017901 (2002).
[35] V. Privman, I. D. Vagner, and G. Kventsel, Phys. Lett. A **239**, 141 (1998).
[36] R. Vrijen, E. Yablonovitch, K. Wang, H. W. Jiang, A. Balandin, V. Roychowdhury, T. Mor, and D. DiVincenzo, Phys. Rev. A **62**, 012306 (2000).
[37] E. L. Hahn, Phys. Rev. **80**, 580 (1950).
[38] H. Y. Carr and E. M. Purcell, Phys. Rev. **94**, 630 (1954).
[39] S. Meiboom and D. Gill, Rev. Sci. Instrum. **29**, 688 (1958).
[40] I. J. Lowe and R. E. Norberg, Phys. Rev. **107**, 46 (1957).
[41] H. Cho, T. D. Ladd, J. Baugh, D. G. Cory, and C. Ramanathan, Phys. Rev. B **72**, 054427 (2005).
[42] O. W. Sorensen, G. W. Eich, M. H. Levitt, G. Bodenhausen, and R. R. Ernst, Prog. Nucl. Magn. Reson. Spectrosc. **16**, 163 (1983).
[43] J. H. Van Vleck, Phys. Rev. **74**, 1168 (1948).
[44] M. Mehring and G. Sinning, Phys. Rev. B **15**, 2519 (1977).
[45] M. M. Maricq, Phys. Rev. B **25**, 6622 (1982).
[46] M. M. Maricq, Phys. Rev. B **31**, 127 (1985).
[47] M. M. Maricq, Phys. Rev. Lett. **56**, 1433 (1986).
[48] D. Sakellariou, P. Hodgkinson, and L. Emsley, Chem. Phys. Lett. **293**, 110 (1998).
[49] D. Sakellariou, P. Hodgkinson, S. Hediger, and L. Emsley, Chem. Phys. Lett. **308**, 381 (1999).
[50] D. Suwelack and J. S. Waugh, Phys. Rev. B **22**, 5110 (1980).
[51] H. C. Torrey, Phys. Rev. **76**, 1059 (1949).
[52] P. A. Keifer, Concepts Magn. Reson. **11**, 165 (1999).
[53] D. Barnaal and I. J. Lowe, Phys. Rev. Lett. **11**, 258 (1963).
[54] I. Solomon, Phys. Rev. Lett. **2**, 301 (1959).
[55] T. Gullion, D. B. Baker, and M. S. Conradi, J. Magn. Reson. (1969-1992) **89**, 479 (1990).
[56] A. J. Shaka, S. P. Rucker, and A. Pines, J. Magn. Reson. (1969-1992) **77**, 606 (1988).
[57] D. I. Hoult, Prog. Nucl. Magn. Reson. Spectrosc. **12**, 41 (1978).
[58] J. D. Jackson, *Classical Electrodynamics*, 3rd ed. (Wiley, New York, 1999).
[59] E. M. Purcell, *Electricity and Magnetism*, Berkeley Physics Course Vol. 2, 2nd ed. (McGraw-Hill, New York, 1985).
[60] J. R. Carson, Philos. Mag. **41**, 607 (1921).
[61] F. E. Terman, *Radio Engineers' Handbook*, 1st ed. (McGraw-Hill, New York, 1943).
[62] D. E. Maclaughlin, Rev. Sci. Instrum. **41**, 1202 (1970).
[63] M. Mehring and J. S. Waugh, Rev. Sci. Instrum. **43**, 649 (1972).
[64] R. W. Vaughan, L. M. Stacey, J. W. Lee, D. D. Elleman, and W. K. Rhim, Rev. Sci. Instrum. **43**, 1356 (1972).
[65] A. J. Vega, J. Magn. Reson. **170**, 22 (2004).
[66] M. D. Hurlimann and D. D. Griffin, J. Magn. Reson. **143**, 120 (2000).
[67] W. X. Zhang, N. Konstantinidis, K. A. Al-Hassanieh, and V. V. Dobrovitski, J. Phys.: Condens. Matter **19**, 28 (2007).
[68] M. H. Levitt, Prog. Nucl. Magn. Reson. Spectrosc. **18**, 61 (1986).
[69] R. Tycko, E. Schneider, and A. Pines, J. Chem. Phys. **81**, 680 (1984).
[70] M. H. Levitt and R. Freeman, J. Magn. Reson. (1969-1992) **33**, 473 (1979).
[71] H. K. Cummins, G. Llewellyn, and J. A. Jones, Phys. Rev. A **67**, 042308 (2003).
[72] S. Wimperis, J. Magn. Reson., Ser. A **109**, 221 (1994).
[73] S. Lee, W. Richter, S. Vathyam, and W. S. Warren, J. Chem. Phys. **105**, 874 (1996).
[74] W. S. Warren, W. Richter, A. H. Andreotti, and B. T. Farmer, Science **262**, 2005 (1993).
[75] E. B. Fel'dman and S. Lacelle, J. Chem. Phys. **104**, 2000 (1996).
[76] S. Lacelle and L. Tremblay, J. Chem. Phys. **102**, 947 (1995).
[77] R. Tycko, R. C. Haddon, G. Dabbagh, S. H. Glarum, D. C. Douglass, and A. M. Mujsce, J. Phys. Chem. **95**, 518 (1991).
[78] C. S. Yannoni, R. D. Johnson, G. Meijer, D. S. Bethune, and J. R. Salem, J. Phys. Chem. **95**, 9 (1991).
[79] A. Allerhand, J. Chem. Phys. **44**, 1 (1966).
[80] S. Hudgens, M. Kastner, and H. Fritzsche, Phys. Rev. Lett. **33**, 1552 (1974).
[81] E. Belorizky, W. Gorecki, M. Jeannin, P. H. Fries, P. Maldivi, and E. Gout, Chem. Phys. Lett. **175**, 579 (1990).
[82] D. C. Cronemeyer, J. Appl. Phys. **70**, 2911 (1991).
[83] L. E. Drain, Proc. Phys. Soc. London **80**, 1380 (1962).
[84] G. Mozurkewich, H. I. Ringermacher, and D. I. Bolef, Phys. Rev. B **20**, 33 (1979).
[85] J. A. Osborn, Phys. Rev. **67**, 351 (1945).
[86] P. V. Sharma, Pure Appl. Geophys. **64**, 89 (1966).
[87] A. Samoson, T. Tuherm, and Z. Gan, Solid State Nucl. Magn. Reson. **20**, 130 (2001).
[88] Yanqun Dong, Dale Li, R. G. Ramos, and S. E. Barrett (unpublished).
[89] U. Haeberlen and J. S. Waugh, Phys. Rev. **175**, 453 (1968).
[90] W. Magnus, Commun. Pure Appl. Math. **7**, 649 (1954).
[91] U. Haeberlen, J. D. Ellett, and J. S. Waugh, J. Chem. Phys. **55**, 53 (1971).
[92] A. Pines and J. S. Waugh, J. Magn. Reson. (1969-1992) **8**, 354 (1972).
[93] J. D. Walls and Y. Y. Lin, Solid State Nucl. Magn. Reson. **29**, 22 (2006).
[94] Yanqun Dong, R. G. Ramos, Dale Li, and S. E. Barrett, Phys. Rev. Lett. **100**, 247601 (2008).
[95] See EPAPS Document No. E-PRBMDO-77-052813 for the movies underlying Figs. 24 and 25. For more information on EPAPS, see http://www.aip.org/pubservs/epaps.html.